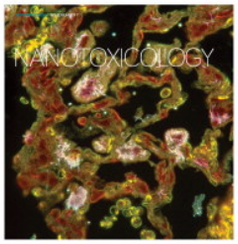

Nanotoxicology

ISSN: 1743-5390 (Print) 1743-5404 (Online) Journal homepage: www.tandfonline.com/journals/inan20

Carbon quantum dots in breast cancer modulate cellular migration via cytoskeletal and nuclear structure

Nikita Dinger, Carmela Russo, Sabato Fusco, Paolo A. Netti, Mariano Sirignano & Valeria Panzetta

To cite this article: Nikita Dinger, Carmela Russo, Sabato Fusco, Paolo A. Netti, Mariano Sirignano & Valeria Panzetta (2024) Carbon quantum dots in breast cancer modulate cellular migration via cytoskeletal and nuclear structure, Nanotoxicology, 18:7, 618-644, DOI: 10.1080/17435390.2024.2419418

To link to this article: https://doi.org/10.1080/17435390.2024.2419418

Published online: 01 Nov 2024.

NANOTOXICOLOGY
2024, VOL. 18, NO. 7, 618–644
https://doi.org/10.1080/17435390.2024.2419418

Taylor & Francis
Taylor & Francis Group

RESEARCH ARTICLE

OPEN ACCESS Check for updates

Carbon quantum dots in breast cancer modulate cellular migration via cytoskeletal and nuclear structure

Nikita Dinger[a], Carmela Russo[b], Sabato Fusco[c], Paolo A. Netti[a,d,e], Mariano Sirignano[a] and Valeria Panzetta[a,d,e]

[a]Dipartimento di Ingegneria Chimica, dei Materiali e della Produzione Industriale, Università degli Studi di Napoli Federico II, Napoli, Italy; [b]Istituto di Scienze e Tecnologie per l'Energia e la Mobilita Sostenibili– CNR – P.le V. Tecchio, Napoli, Italy; [c]Department of Medicine and Health Sciences 'V. Tiberio', University of Molise, Campobasso, Italy; [d]Interdisciplinary Research Centre on Biomaterials, CRIB, University of Naples Federico II, Naples, Italy; [e]Center for Advanced Biomaterials for HealthCare IIT@CRIB, Istituto Italiano di Tecnologia, Naples, Italy

ABSTRACT

Carbon nanomaterials have been widely applied for cutting edge therapeutic applications as they offer tunable physio-chemical properties with economic scale-up options. Nuclear delivery of cancer drugs has been of prime focus since it controls important cellular signaling functions leading to greater anti-cancer drug efficacies. Better cellular drug uptake per unit drug injection drastically reduces severe side-effects of cancer therapies. Similarly, carbon dots (CDs) uptaken by the nucleus can also be used to set-up cutting edge nano delivery systems. In an earlier paper, we showed the cellular uptake and plasma membrane impact of combustion generated yellow luminescing CDs produced by our group from fuel rich combustion reactors in a one-step tunable production. In this paper, we aim to specifically study the nucleus by establishing the uptake kinetics of these combustion-generated yellow luminescing CDs. At sub-lethal doses, after crossing the plasma membrane, they impact the actin and microtubule mesh, affecting cell adhesion and migration; enter nucleus by diffusion processes; modify the overall appearance of the nucleus in terms of morphology; and alter chromatin condensation. We thus establish how this one-step produced, cost and bulk production friendly carbon dots from fuel rich combustion flames can be innovatively repurposed as potential nano delivery agents in cancer cells.

GRAPHICAL ABSTRACT

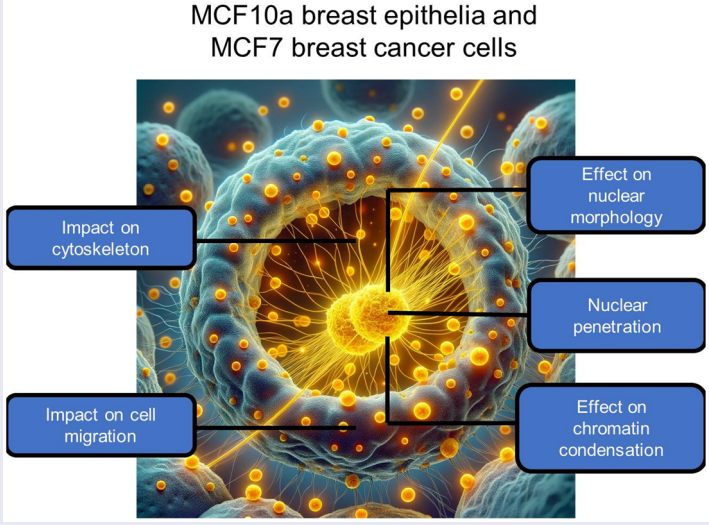

ARTICLE HISTORY
Received 28 February 2024
Revised 2 October 2024
Accepted 16 October 2024

KEYWORDS
Breast cancer; carbon dots; cell migration; cytoskeleton; nuclear uptake

CONTACT Mariano Sirignano mariano.sirignano@unina.it Dipartimento di Ingegneria Chimica, dei Materiali e della Produzione Industriale, Università degli Studi di Napoli Federico II, Napoli, Italy

1. Introduction

It is important to note that while there are several targeted therapies available for specific types of breast cancer, there is an ongoing need for novel treatment strategies, such as the use of Carbon dots (CDs). CDs have shown potential in improving the specificity and efficacy of cancer treatments through their unique optical and electronic properties, biocompatibility, and ability to be functionalized with various therapeutic agents. These nanomaterials offer a promising avenue for enhancing drug delivery, imaging, and therapeutic outcomes in breast cancer care. They also show promise as carriers for drugs to overcome this challenge, offering improved stability and better tissue penetration compared to conventional methods (Agostinetto, Gligorov, and Piccart 2022).

In the context of nanoparticles, carbon-based ones have become a focus for drug delivery since the discovery of multiwall carbon nanotubes, offering tunable properties. These materials have low cytotoxicity and small sizes, making them suitable for precise targeting of subcellular organelles. CDs, a type of 0D carbon material, have gained popularity for their small size, high surface area, continuous absorption spectra, narrow emission spectra, and photochemical stability within carbon nanomaterials (Ji et al. 2020; Kour et al. 2020; Saini et al. 2021; Wareing, Gentile, and Phan 2021).

CDs have widespread use in intracellular applications of drug delivery. Efficient drug loading onto quantum dots can be achieved by thoroughly understanding their effects on cells, including cytotoxicity, targeted intracellular dynamics, and genotoxicity (Biswas et al. 2021; Lee et al. 2019; Liu et al. 2008; Xiao et al. 2010). For cancer therapies, genotoxic effects are particularly being studied to investigate extensively if CDs can be directed to the cell nuclei to destroy flawed genetic material and enhance anti-tumor therapy (Abuetabh et al. 2022; Carneiro and El-Deiry 2020; Huang and Zhou 2021; Tanaka et al. 2009; Torgovnick and Schumacher 2015). Researchers are focusing on understanding cytoskeletal dynamics to combat tumor migration and metastasis. Nano-scale materials are being used to disrupt this network, but targeting subcellular regions remains challenging due to limited research on nanoparticle-cell interactions (Naik et al. 2022). Photo-induced tumor therapies require imaging agents with high absorption coefficient in the biological window (650–900 nm). This feature makes CDs a very promising candidate for cancer therapies (Guo et al. 2022). Also, to target brain tumors, the blood-brain barrier needs to be penetrated for which CDs of smaller sizes are being explored. However, given their tedious traditional productions, an eco-friendly, biocompatible, biodegradable, cost-effective, one-step synthesis with possibility of bulk industrial production is an urgent need of the times to develop innovative and low-cost cancer therapies (Desai 2012).

Our group recently established a one-step simple and economical production of tunable luminescent CDs from fuel rich combustion reactors (Sirignano, Russo, and Ciajolo 2020). During incomplete combustion, fossil fuels emit gaseous byproducts such as high molecular weight polycyclic aromatic hydrocarbons and particulate matter (characterized by a bi-modal size distribution of nanoparticles 1–5 nm and soot 10–100 nm) (Pedata et al. 2015; Sirignano et al. 2018). Using yellow luminescing CDs we had explored in our previous work, the intracellular uptake, expulsion kinetics and sequestration over 24 hours after uptake (Dinger et al. 2022). We had observed heterogeneous populations of CDs in MCF7 breast cancer cells. One subset comprised nearly 20% of the uptaken CDs and was entrapped in late endosomes and lysosomes, while the remaining population subset appeared freely diffused in the cytoplasm. It was noticed that approximately 20% of the CDs were retained in the cytoplasm when given a 24-hour recovery period. Overall, these CDs increased membrane stiffness, affected cellular morphology and decreased cellular vitality.

Nonetheless, there remains a significant gap in our understanding of the intracellular pathways that CDs activate, especially for carriers designed for transporting genes, drugs, and contrast agents, to intracellular organelles like the nucleus. A detailed study of CD fate within cells is imperative to successfully utilize them for targeted intracellular delivery. For this, we have already demonstrated that a relevant, but not prevailing percentage of CDs (~20%) can be retained in the cytoplasm after entering tumor cells. by endocytic pathway, being retained in the cytoplasm over a long time. Taking into account the pivotal role of the cytoskeleton in mediating long-range endocytosis-associated transport of cargoes within the cell, an open question concerns its involvement in the process of CD uptake. More importantly, the cytoskeleton by means of its physical connection to the nuclear envelope mediated by the LINC (Linker of Nucleoskeleton and Cytoskeleton) complex, has a relevant impact on transport of CDs and

nanoparticles in general up to the nucleus (Davidson and Cadot 2021; Grady et al. 2017; JayaNandanan, Mathew, and Leptin 2014; Olson and Nordheim 2010). Due to its pivotal role in governing cellular functions, including reproduction, metabolism, growth, and apoptosis, the nucleus stands as a drug target of paramount importance. In cancer cells, nuclear architecture shows alterations leading to changes in the shape and spatial organization of the genome and nuclear components. The chromatin texture changes as a result of oncogene activation (Zink, Fischer, and Nickerson 2004). In this context, nano-sized materials, including quantum dots and gold spheres, are being explored for their potential in targeting organelles, among which the cytoskeleton itself, and the nucleus for therapeutic purposes (Fu et al. 2020; Latha et al. 2023; Murciano-Goroff et al. 2020; Rozenblatt-Rosen et al. 2020; Stratton 2011; Wang et al. 2020; Zhang, Alisafaei, et al. 2020). In fact, targeting the delivery of small nanoparticles into subcellular structures by crossing tightly-regulated membranes with small pore sizes has opened the possibility of new therapeutic paths such as organelle-specific modulation and direct drug delivery (Cheng et al. 2008; Kang, Mackey, and El-Sayed 2010; Raoof et al. 2012). As mentioned, the nucleus is a highly desired target for DNA delivery (during gene therapy) and small drug delivery (for stalling DNA activity and also causing its damage). Since the pore of the nuclear membrane has strict dimensions, numerous types of small nanoparticles (less than 20 nm diameter) have been synthesized and coupled with other biocompatible molecules (Barhoum et al. 2022). Typical materials have included quantum dots, fullerenes, gold spheres and nanohorns.

In the first part of this paper, we have examined the role of the cytoskeleton in mediating the intracellular uptake of sub-lethal doses of CDs (derived from our previous work) (Dinger et al. 2022). Given their size (<5nm), we explored CD entrapment in the actin and tubulin mesh networks within the cell through colocalization studies. At the same time, we have investigated the structural and functional effects of CD uptake on the cytoskeleton. In particular, we have investigated the structural effects on two cytoskeletal polymers: actin and β-tubulin. From a functional perspective, given the crucial role of the cytoskeleton in regulating various cellular functions, including cell adhesion and migration, our research has focused on investigating the impact of CD uptake on the morphology of focal adhesions (FAs). FAs are adhesive plaques that establish a structural link between the external cellular environment and the internal cytoskeleton, thereby influencing cell migration. In order to establish the relevance of the cytoskeleton dynamicity, we compare the uptake rates in metabolically viable cells and low-temperature paused cells to investigate the role of cytoskeletal contractility. In the second part of this paper, we have examined nuclear uptake kinetics and retention while also studying their functional effects on nuclear morphology and genotoxic chromatin condensation. Figure 1 illustrates the workflow of the paper.

We thus have explored in detail the subcellular effects of CD uptake on breast cancer and normal breast epithelia (MCF7 and MCF10a, respectively). These foundational studies open up the possibility of using these economical, easy to bulk produce and tunable small CDs as penetrative, nuclear targeting agents, which degrade tumor cell cytoskeleton and slower tumor migration rates. A detailed study like this highlights the need for further research in the area of specific cell-particle interactions, which is a critical gap in the current literature on CD research. By addressing this gap, we can better understand the mechanisms underlying CD-cell interaction and develop more effective treatment strategies (Desai 2012; Mitchell et al. 2021).

2. Results and discussion

2.1. CD uptake shows effects on cell migration during 24 h

Following our previous findings indicating consequential alterations in cell morphology and cell division in our earlier investigations, we are here interested in evaluating the feasibility of employing CDs to inhibit cancer metastasis and progression (Dinger et al. 2022; Gonciar et al. 2019; Zhang et al. 2021). Furthermore, there exists the possibility that our small CDs would sit in the open pores of actin filaments (the open pore size and thickness of whom is variable and subject to extracellular factors) and hence interfere with the tumor cell structure, as partly demonstrated by the effects observed on breast cells (Dinger et al. 2022; Rother et al. 2015; Svitkina 2020).

To elucidate the impact of CDs on cell morphology and their subsequent influence on cell migration, a time lapse video analysis was performed for MCF10a and MCF7 cells in control conditions, with a positive control by using specific drugs (Cytochalasin D and Nocodazole) and during

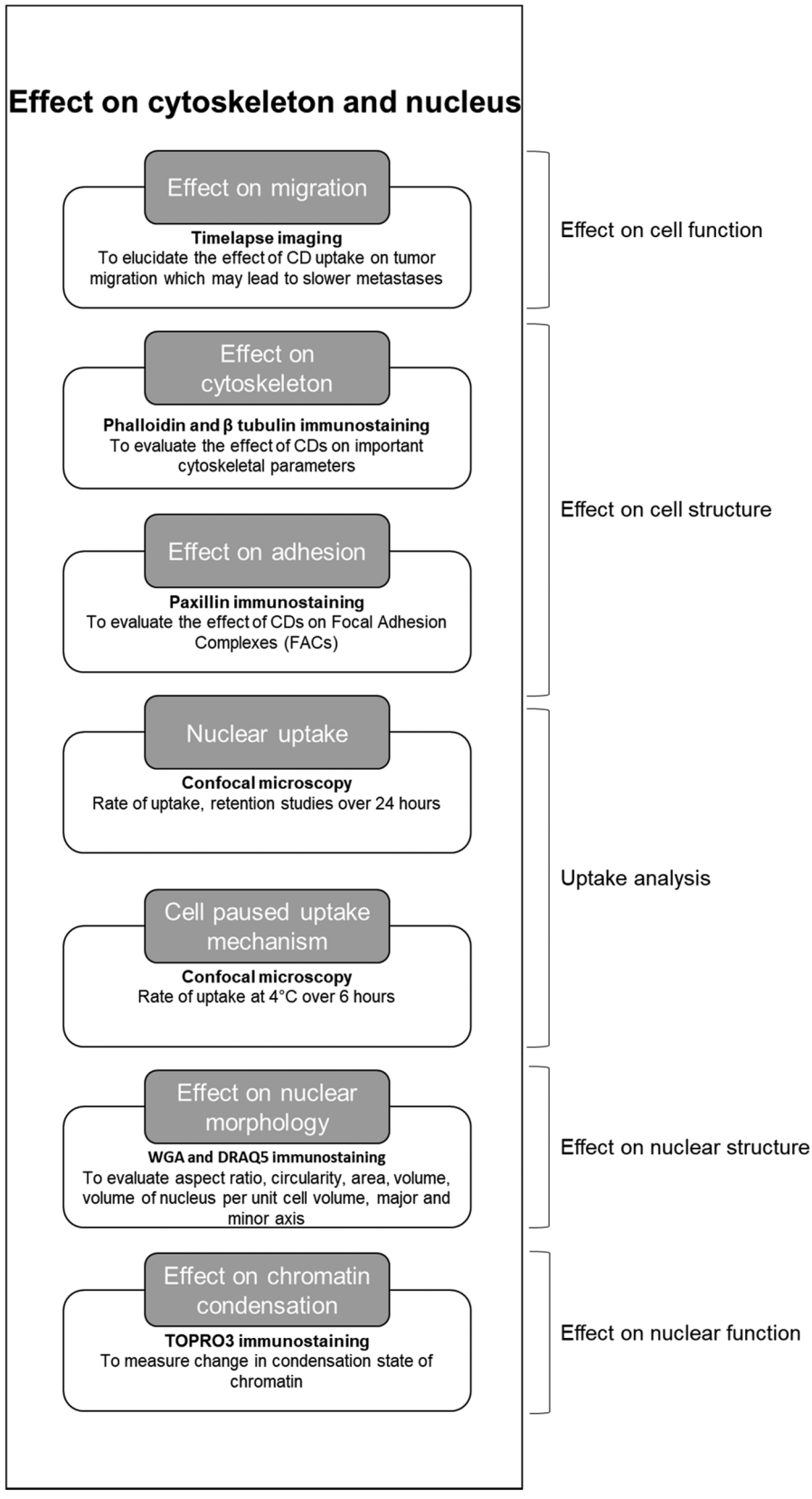

Figure 1. Schematic representation of workflow.

exposition to CDs. In fact, in order to understand if the effects produced by CDs can be ascribed to cytoskeleton modification, cells were treated with Cytochalasin D and nocodazole. The primary objective of this experiment was to investigate the mechanism by which cells control directional persistence

during migration. For this purpose, we performed both qualitative and quantitative analysis on the trajectories the cells followed over about 24 h. Figure 2 shows the cell trajectories translated into the origin. In control conditions, MCF7 cells show greater displacements compared to MCF710a cells (Figure 2(A,E)), a typical characteristic of tumor cells (Geltmeier et al. 2015; Lee et al. 2012). Cytochalasin D and nocodazole treatment strongly reduced cell movement in both MCF10a and MCF7 cell lines which show restricted movement mainly localized around their point of origin. Exposure to CDs did not affect in a significant way MCF10a motility, whereas MCF7 cells strongly reduced their displacements.

Quantitatively, cell motility was characterized by analyzing two parameters: the average velocity as a kinematic parameter integrated over time (total migration path length divided by total time) and the chemotactic index (Hu, Becker, and Willits 2023). It is worth noting that in previous investigations, it was established that cells exhibited a linear uptake of CDs up to 6 h after which the saturation was reached (Dinger et al. 2022). To assess whether CD uptake affected cell motility differently during the first 6 hours compared to the following 18 hours,

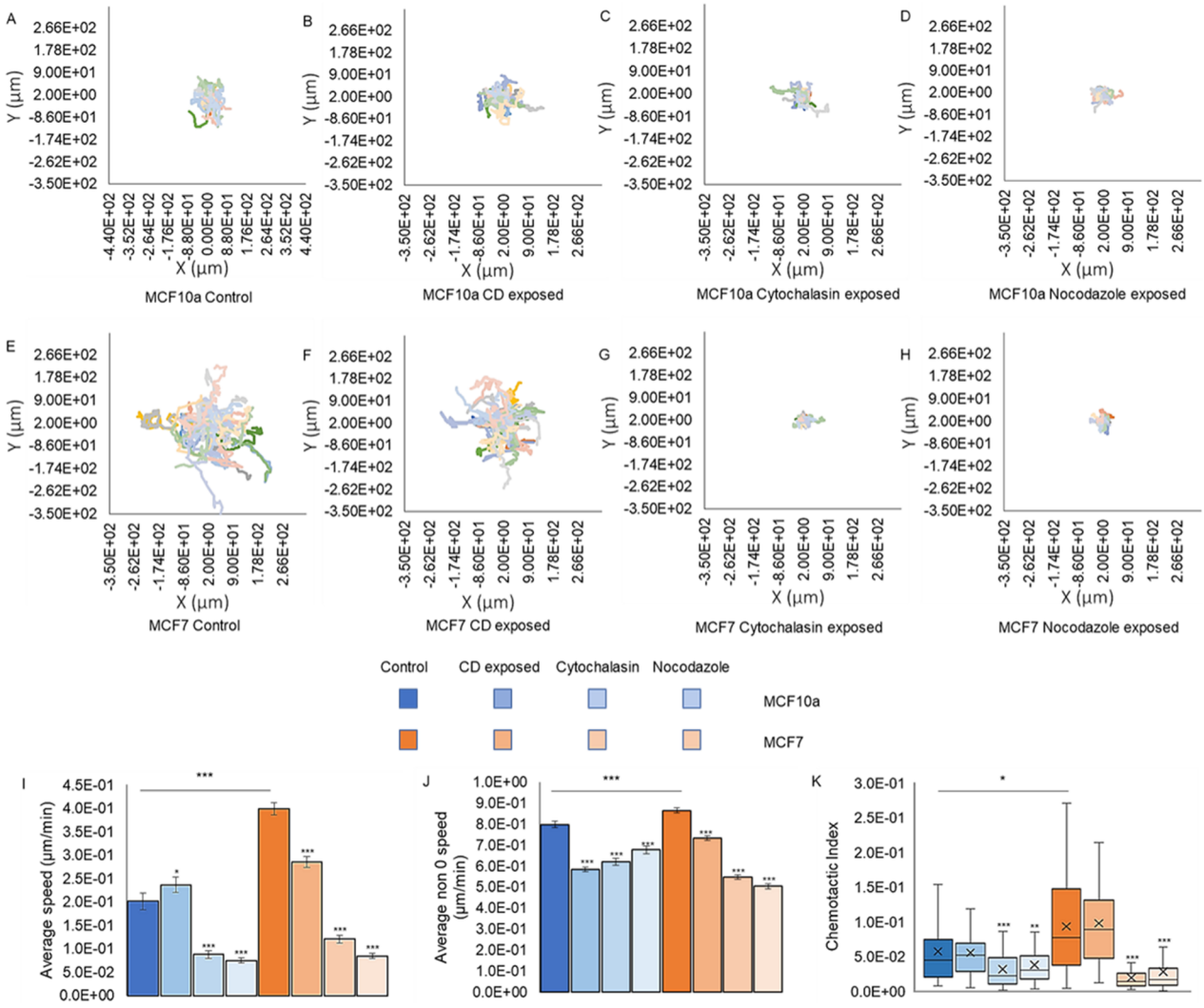

Figure 2. Panels (A–H): cell trajectories translated to the origin: Comparison of MCF7 and MCF7-10a cells illustrating the trajectories of cell movement with translations to the origin, highlighting the distinct behavior of MCF7 and MCF7-10a cells under control conditions. Time of exposure: ~0 to 24 h (I) MCF10a healthy cells show an increase in velocity while MCF7 tumor cells show a decrease in their velocity. (J) When calculated for non-0 speed, MCF10a healthy cells and MCF7 tumor cells show a decrease in their velocity similar to positive drug treated controls. (K) the chemotactic index of cells is <0.1, showing random directionality for both MCF10a and MCF7. MCF10a is depicted in blue and MCF7 in brown. (A–H) Graphs are represented as scatter plots, tracing the cell path in microns along X and Y axes. (I–K) Data are represented as a bar graph with capper heads marking deviations, and boxes representing quartile range. Mean is represented as the Central solid line. $p < 0.05$; $p < 0.01$; $p < 0.001$ with respect to control.

cell velocity was analyzed hourly. The analysis showed no significant difference in cell velocity between these two time intervals. However, when considering the average cellular velocity over 24 hours, MCF10a cells exhibited significantly lower speeds than MCF7 cells. Exposure to CDs increased the average speed by 16.58% in MCF10A cells and decreased it by 28.36% in MCF7 cells (Figure 2(I)).

Regardless of the condition and cell line, cell trajectories included periods of immobility, with MCF10a cells showing a higher percentage of still motions (74.68%) compared to MCF7 cells (53.93%). Excluding still motions, average cell velocities were higher in tumor cells but closer to each other compared to average velocities including still motions. CD uptake significantly affected non-zero velocity, reducing still motions in MCF10a cells and increasing them in MCF7 cells.

Interestingly, the effects of CDs on MCF7 cells were reversed when considering non-zero velocity instead of average velocity, indicating reduced movement despite fewer still motions (Chen, Yan, and Chen 2023). Treatment with Cytochalasin D and nocodazole significantly lowered average velocities in both cell lines compared to control conditions and cells exposed to CDs, highlighting the importance of the cytoskeleton in cell migration. However, non-zero velocities were not significantly different between cells treated with drugs and those exposed to CDs, suggesting that the number of still movements is more critical than the value of non-zero velocity in assessing cell motility.

Directional persistence, a crucial parameter in cell migration efficiency, measures the time a cell takes to change its direction during movement. Lamellipodial protrusions and cellular tail stabilizations influence directional persistence. Tumor cells typically exhibit increased velocity and persistence due to their reduced mechanical stiffness, allowing them to maintain polarity better and, consequently, invade and form metastases (Panzetta, Verde, et al. 2020; Liu et al. 2020). Considering the clinical significance of directional persistence, we evaluated the effect of CD uptake on this migratory parameter. Directional persistence was assessed through the chemotactic index, which measures the degree of directionality exhibited by a cell. A chemotactic index of 1 indicates straight line motion, while 0 indicates random cell motion. Additionally, we calculated the mean squared displacement (MSD, Supplementary Figure 1), a physical parameter that measures the surface areas explored by cells over time, providing insight into their migration efficiency, including both speed and directional persistence. The α-values derived from the slope of log-log MSD graphs indicate the cell's mode of migration, with values close to 1 indicating random Brownian motion, <1 indicating constricted motion, 0 indicating still cells, >1 indicating super-diffusive migration, and ~2 indicating cells being propelled by a convective force and moving in a straight line (Gorelik and Gautreau 2014). Under control conditions, MCF10a cells exhibited MSD slopes slightly lower than 1 (Figure 2(J)), indicating marginally sub-diffusive motion, while MCF7 cells displayed slopes greater than 1, suggesting super-diffusive motion. Similarly, MCF10a showed a lower chemotactic index than MCF7, as a consequence of their low propensity to move directionally (Figure 2(K)). However, both cell lines showed low chemotactic indices (<0.3), signifying little directional movement during migration.

Upon exposure to CDs, both MCF10a and MCF7 CD-exposed cells did not show any significant change in their chemotactic index with respect to corresponding controls (Figure 2(K)). As for the α-values (Supplementary Table 1), after exposure to CDs, MCF10a decreased from 1.16 to 1.07 (with R^2 increasing from 0.99 to 1.00), while in MCF7, the α-value increased from 0.83 to 0.90 after exposure (with R^2 decreasing from 1.00 to 0.98).

Upon treatment with Cytochalasin D and Nocodazole, the amplitude of MSDs in both cell lines were considerably reduced (Supplementary Figure 1), as was the average velocity, whereas the α-values were not affected in MCF7 but increased in MCF10a. The chemotactic indices reduced significantly, approximating to zero when the movement is almost completely inhibited as a consequence of the cytoskeleton destruction (Melzer, von der Ohe, and Hass 2019; Blajeski et al. 2002).

Few studies on this aspect have been found in literature for other nanoparticle exposures. In HEYA8 ovarian epithelial tumor cells, exposure to nuclear-targeted gold nanorods measuring 25 (±2) × 5 (±0.5) nm did not yield any evident changes in the migration coefficient (Ali et al. 2017). Conversely, In NCI-H292 cells exposed to pegylated titanium dioxide nanoparticles, and slower migration was observed which further decreased with larger nanoparticles (Sun, Kanehira, and Taniguchi 2018). To the best of our knowledge, this is the first work which shows that such small carbon quantum dots of ~2 nm lead to a reduced migration rate, hinting at their potential future application therapeutic antitumor agents (Alexandrova and Lomakina 2022; Gallaher, Brown, and Anderson 2019; Schliwa 1982).

2.2. CD uptake impacts actin and microtubule network

The cytoskeleton plays a crucial role in providing structural support to the cell, acting as a scaffold to maintain cell shape, organize subcellular compartments, and control cargo trafficking to organelles. Composed of actin filaments, microtubules, and intermediate filaments, this network operates in a highly regulated manner to control essential functions such as cell migration, organelle transport, and chromosome segregation during cell division. Without a healthy cytoskeleton, these processes cannot occur efficiently (Kim and Coulombe 2010; Tang and Gerlach 2017). Specifically, both the actin cytoskeleton and microtubules are involved in the coordination of cell motility. The actin filaments power the cell movement by means of contractile forces generated by myosin motor activity (Kasza and Zallen 2011). Microtubules regulate actin dynamics and provide for cell polarization during migration (Kaverina and Straube 2011).

Considering the migration data and the structural impact of carbon dots (CDs) on actin filaments and microtubules, we analyzed their effects on MCF10A and MCF7 cells (Figure 3 for F-actin and Figure 4 for β-tubulin). A reduction in phalloidin intensity was observed in both MCF10a and MCF7 (19.68 and 31.35%, respectively), while β-tubulin showed a 94% increase in fluorescence intensity in MCF10a cells and a 36% decrease in MCF7 cells.

These results explain the differential migration rates, where MCF10a showed an increase in average velocity while MCF7 showed a decrease over 24 hours. The partial destruction of F-actin in MCF10A may reduce acto-myosin activity necessary for cell motility (T, 2018). However, this seems compensated by the increased level of β-tubulin and possibly an increase in kinesin motor activity, which regulates lamellipodial activity, controlling cell asymmetry and migration (Kaverina and Straube 2011). Other uninvestigated proteins may have also contributed to this behavior. We also introduced negative controls using Cytochalasin D to assess phalloidin destruction and nocodazole to assess tubulin destruction, as detailed in Supplementary Figures 7 and 8, respectively. The cells treated with Cytochalasin D showed severely destroyed actin cytoskeleton and the accumulation of foci composed of short actin filaments that contribute to the increased fluorescence (Supplementary Figure 7) (Irianto, Lee, and Knight 2014). The cells treated with nocodazole exhibit a significant reduction in β-tubulin levels compared to the unexposed CD controls (Supplementary Figure 8).

We aimed to confirm the direct interaction of CDs with actin and β-tubulin by investigating their co-localization. After 24 hours of exposure, CDs were found to be organized in ordered structures similar to actin filaments and microtubules.

The Meander's correlation coefficient was calculated to assess the degree of co-localization, with values of 1.00 indicating complete co-localization and 0.00 indicating none. In MCF10a cells, the coefficient for CDs masked on phalloidin (M1) was 0.46, and for phalloidin masked on CDs (M2) was 0.35. In MCF7 cells, M1 was 0.58 and M2 was 0.49, suggesting that actin filaments were mainly localized where CDs were present, though not all CDs were trapped by the actin cytoskeleton.

Similarly, for β-tubulin, in MCF10a cells, M1 was 0.80 and M2 was 0.91, and in MCF7 cells, M1 was 0.99 and M2 was 0.71 in the blue channel, indicating high co-localization between CDs and β-tubulin proteins. This suggests that most CDs and β-tubulin proteins are highly co-localized with each other.

These findings indicate that CDs interact with actin and β-tubulin, possibly resulting in partial disruption of the actin cytoskeleton and correlating well with changes in cell morphology and division observed in previous research (Dinger et al. 2022; Barooji et al. 2021).

The continuous polymerization and depolymerization of actin fibers controlled by the cytoskeleton are vital for cell stability. Our CDs effectively interact with the cell's internal structure, reducing tumor cell migration over 24 hours. This ability of CDs to disrupt cell morphology, reduce division, and slow down MCF7 cells is remarkable and holds promise for future applications. Since both actin and tubulin are dynamic polymers, CD binding is expected to disrupt the polymerization activity of the cytoskeletal network and promote cell instability (Fletcher and Mullins 2010; Nakaseko and Yanagida 2001).

2.3. CD migration is influenced via focal adhesions

Transmembrane integrin receptors and intracellular proteins like paxillin (PAX), focal adhesion kinase (FAK), and vinculin (VCL) form focal adhesions (FAs). FAK regulates actin and microtubules, controls cell signaling, and recruits other proteins. PAX interacts with FAK and VCL, affecting the actin cytoskeleton, proliferation, and adhesion. VCL interacts with actin,

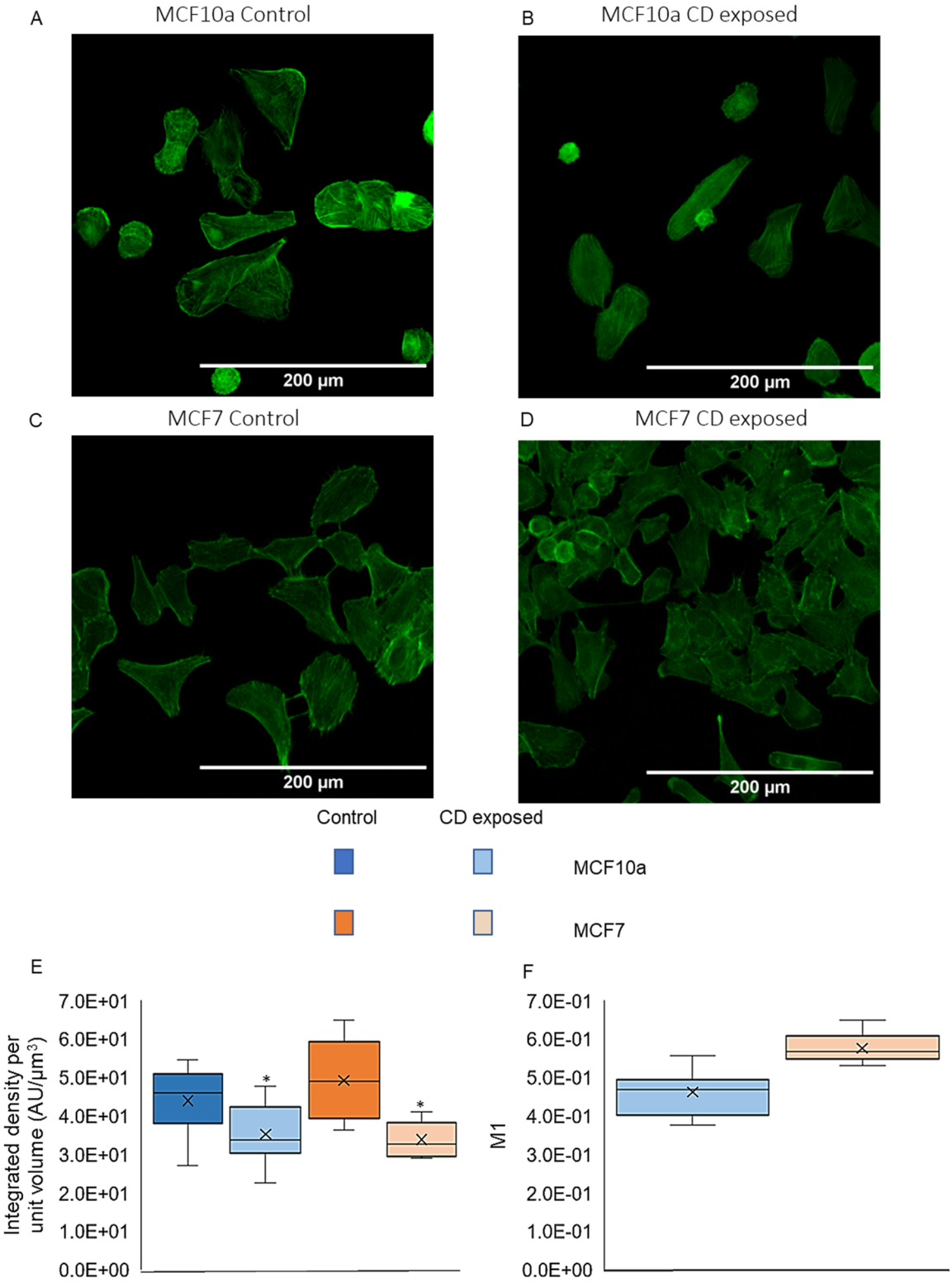

Figure 3. (A–D) Confocal images of MCF10a (top) and MCF7 (bottom) cells showing the destruction of the actin cytoskeleton. The cells were stained for F-actin fibers with phalloidin and imaged in the far red channel. Scale bar= 200 µm. (E) Quantified destruction of F-actin density upon CD exposure. (F) Colocalization of CDs and phalloidin increases over 24 h indicating the increase in entrapment of CDs in the actin meshwork. MCF10a is depicted in blue and MCF7 in brown. Data are represented as a box and scatter plot with capper heads marking deviations, and boxes representing quartile range. Mean is represented as the central solid line. $p < 0.05$; $p < 0.01$; $p < 0.001$ with respect to control.

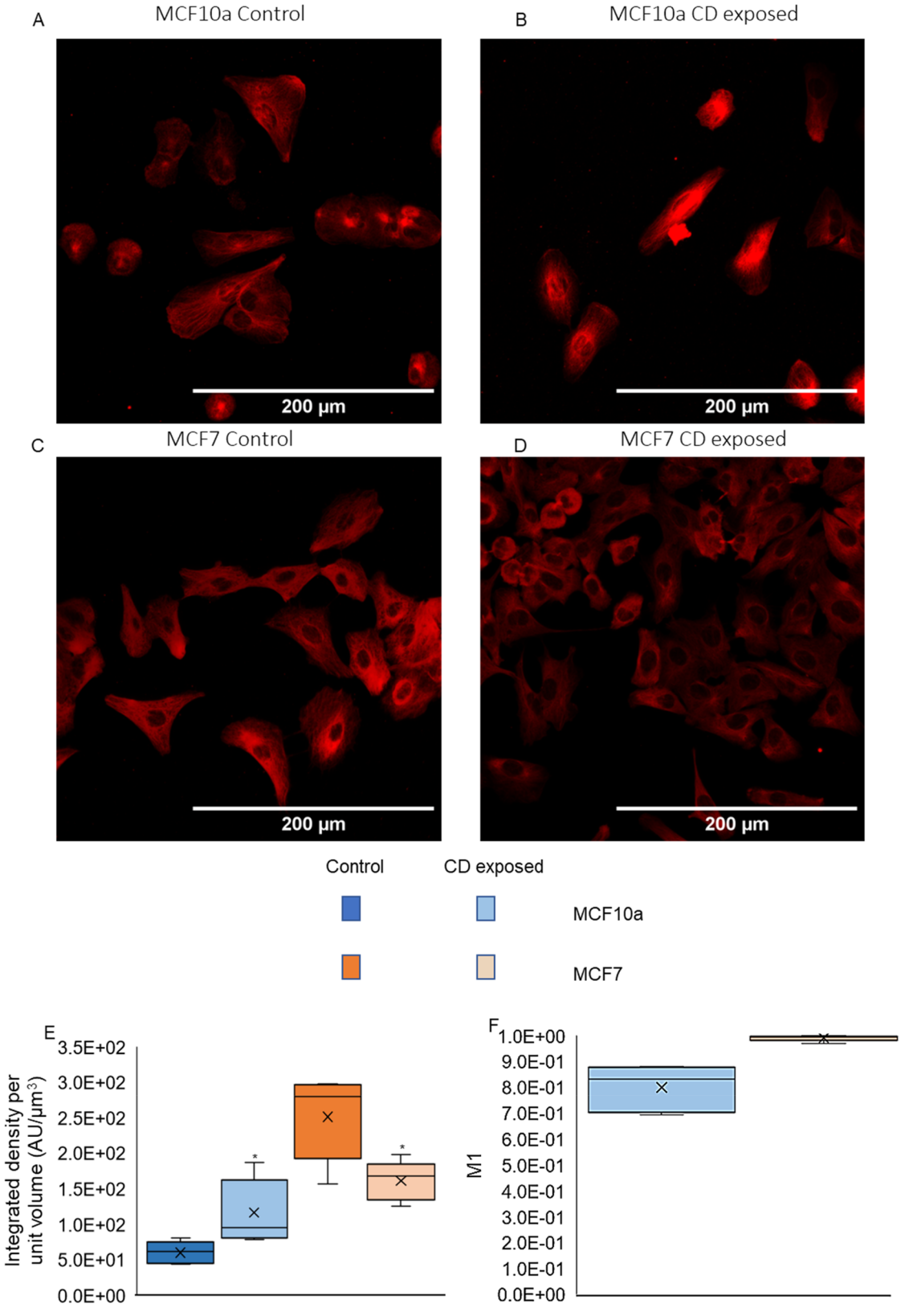

Figure 4. (A–D) Confocal images of MCF10a (top) and MCF7 (bottom) cells showing the destruction of the β-tubulin network. Scale bar = 200 µm. (E) CD exposure increases β-tubulin polymerization in MCF10a and destroys the network in MCF7. (F) Colocalization of CDs and β-tubulin over 24 h indicating the entrapment of CDs in the actin meshwork. MCF10a is depicted in blue and MCF7 in brown. Data are represented as a box and scatter plot with capper heads marking deviations, and boxes representing quartile range. Mean is represented as the central solid line. $p < 0.05$; $p < 0.01$; $p < 0.001$ with respect to control.

tensin, and PAX to control cell morphology, adhesion, and growth. Up-regulation of these proteins increases FAs, modifies the cytoskeleton, and regulates migration. FAs link intracellular actin to the extracellular matrix, enhancing anchorage and modulating signaling (Fletcher and Mullins 2010; Burridge 2017; Geiger, Spatz, and Bershadsky 2009). To evaluate the effect of focal adhesions on cell migration and to gain a better understanding of the data observed in Section 2.1, we studied FAs by staining for PAX.

The adhesiveness of cells at the focal adhesion (FA) scale was evaluated by measuring the normalized area of FAs on cell spreading area (Figure 5(E)) and morphological parameters of single FAs (area, major and minor axis). In MCF10A cells exposed to CDs, the total area occupied by FAs increased, though not significantly, while their morphological features were reduced. Conversely, MCF7 cells showed a non-significant reduction in the normalized area of total FAs, with no effect on their morphological parameters after CD exposure.

The increase in normalized area of FAs coupled with their reduced dimensions in MCF10a cells suggests an increase in the number of FAs per cell after CD uptake, making them more dynamic and potentially more motile. However, the decrease in the average dimensions of FAs may lower the local propulsive forces necessary for migration, resulting in reduced average non-zero velocity and chemotactic index (CI).

In MCF7 cells, the reduction in the normalized area of FAs led to a global reduction in adhesion/propulsive force, resulting in decreased average velocity and non-zero velocity.

The overall functional effects of CDs result from a combination of various signaling factors and heterogeneous polymers constituting the cytoskeleton. Each protein may interact differently with CDs (Wen and Janmey 2011; Behzadi et al. 2017). In our observations, CDs appeared to have a more pronounced effect in disrupting the FACs of healthy MCF10a cells than in the case of MCF7 tumor cells. When focal adhesions were treated with Cytochalasin D as a control (Supplementary Figure 9), paxillin mainly becomes cytoplasmic, not serving as a good control and impeding quantitative analysis.

While CDs disrupted structural elements of phalloidin, they had differential effects on cell migration in both cell lines and promoted microtubule network formation in MCF10a, resulting in a net positive outcome. This is similar to findings with small silver nanoparticles (AgNPs) that can destroy the cytoskeleton, affect membrane roughness, and reduce cell adhesion and stiffness in colon cancer cells (Xiao, Chen, and Alnaggar 2019).

In another study with CDs (diameter 3.97 nm) derived from curcumin and ethylenediamine, it was found that they impeded cell migration, with only 25% of human dermal fibroblast cells retaining motion, while also disrupting the actin and tubulin network (Chittasupho et al. 2021).

2.4. CDs were up taken by the nucleus linearly up to 6 h and showed a saturation till 24 h

As previously discussed, both actin filaments and microtubules showed great affinity with CDs and a large amount of literature revealed the pivotal role of microtubules in endocytic trafficking and in particular in mediating the transport of the endocytic content from early to late endosomes (Elkin, Lakoduk, and Schmid 2016). Actin filaments are involved in various types of endocytosis and vesicle movement within cells. Our recent research indicates that CDs enter cells through active transport pathways, ending up in endo-lysosomes. Actin filaments, along with microtubules and motor proteins, facilitate the movement of these CDs toward the nucleus, aiding in nuclear uptake. Preliminary images suggest CDs can enter the nucleus by infiltrating the nuclear membrane, possibly through water channels (Fahrenkrog and Aebi 2003; Hinshaw, Carragher, and Milligan 1992; Stoffler, Fahrenkrog, and Aebi 1999; Wang and Brattain 2007). In our case, the small size of the CDs is a crucial factor that can allow them to similarly move into the nucleus differentiating them from larger nanoparticles.

Particularly in MCF7 breast cancer cells, small gold nanoparticles of 2 nm and 6 nm have shown to enter the nucleus while particles larger than 10 nm could not enter (Huo et al. 2014). Similarly, in 48 h, TiO_2 (titania) and/or α-FeO(OH) (goethite) nanoparticles were shown to enter lung epithelial cells (A549) with 40% nuclear localization. The size of these particles was bimodally distributed with the peaks centered at 18 nm and 190 nm for α-FeO(OH), and 28 nm and 290 nm for TiO_2 (Ahlinder et al. 2013).

Figure 6 illustrates the nuclear uptake of CDs, which reached saturation at around 6 hours of exposure in both MCF7 and MCF10a cells. In MCF7 cells, nuclear uptake was 1.5 to 2.5 times greater than in MCF10a cells. After a 24-hour recovery period, approximately 20% of CDs in MCF10a and 17% in MCF7 were retained in the nucleus. The

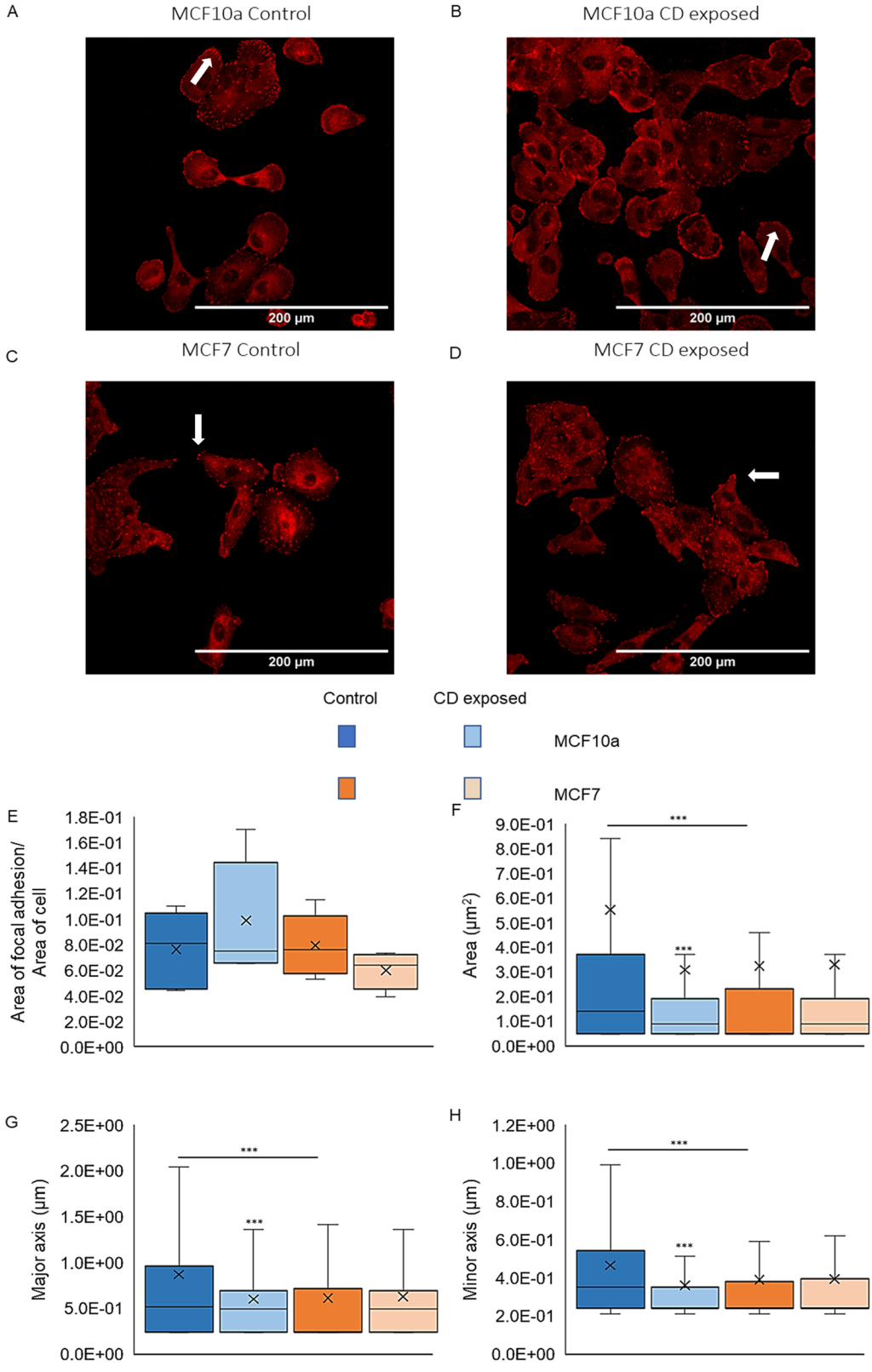

Figure 5. (A–D) Confocal images of MCF10a (top) and MCF7 (bottom) cells showing the effect on paxillin in FACs. Scale bar= 200 µm. (E–H) CD exposure affects FACs in both MCF10a (blue) and MCF7 (brown) by increasing the area of FACs (top left, ns), major axis (Middle left) and minor axis (Middle right), in MCF10a. The area of focal adhesion per unit cell area (bottom left) increases in MCF10a and decreases in MCF7, even if not in a significant manner. MCF10a is depicted in blue and MCF7 in brown. Data are represented as a box and scatter plot with capper heads marking deviations, and boxes representing quartile range. Mean is represented as the Central solid line. $p < 0.05$; $p < 0.01$; $p < 0.001$ with respect to control.

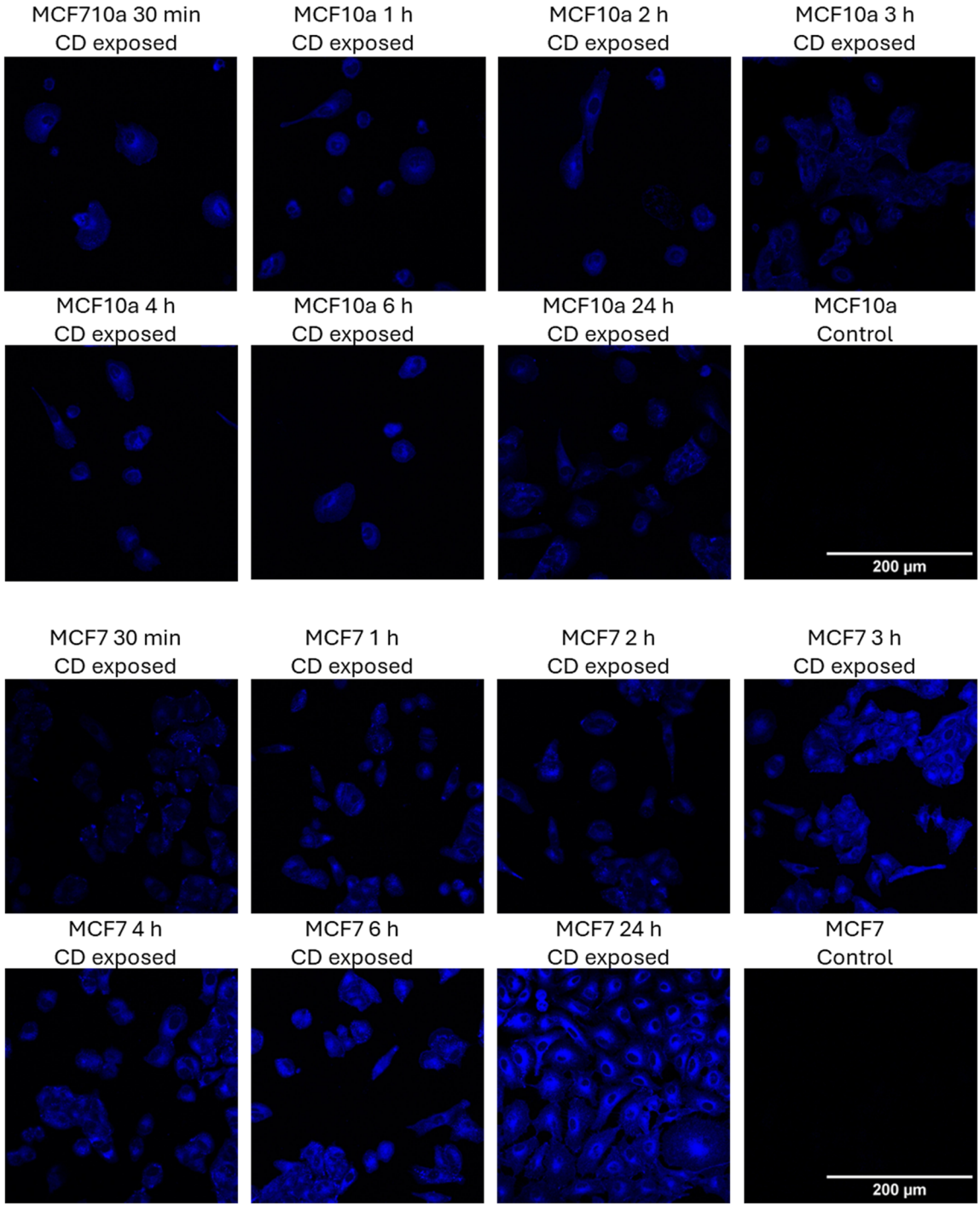

Figure 6. Panel A–B: Confocal images of MCF10a (A) and MCF7 (B) cells showing penetration of CDs into the nucleus. Scale bar= 200 µm. (C–F) CDs show a linear uptake until 6 h and thereafter a saturation until 24 h in MCF10a (blue, top left) and MCF7 (brown, top right). Both cell lines retained the CDs even when allowed a recovery time of 24 h in fresh media (MCF10a blue, bottom left and MCF7 brown, bottom right). Data are represented as a box and scatter plot with capper heads marking deviations, and boxes representing quartile range. Mean is represented as the Central solid line. $p < 0.05$; $p < 0.01$; $p < 0.001$ with respect to control.

nuclei were then isolated to be measured independently from the extra-nuclear components. The CD intensities of isolated nuclei were measured similar to nuclei inside cells, thus confirming the data (Figure 7).

The observed disparity in CD uptake between MCF7 and MCF10a suggests potential variations in their effects on these cell types. Tumor cells, with altered metabolism and dysregulated signaling pathways, may exhibit distinct intracellular trafficking

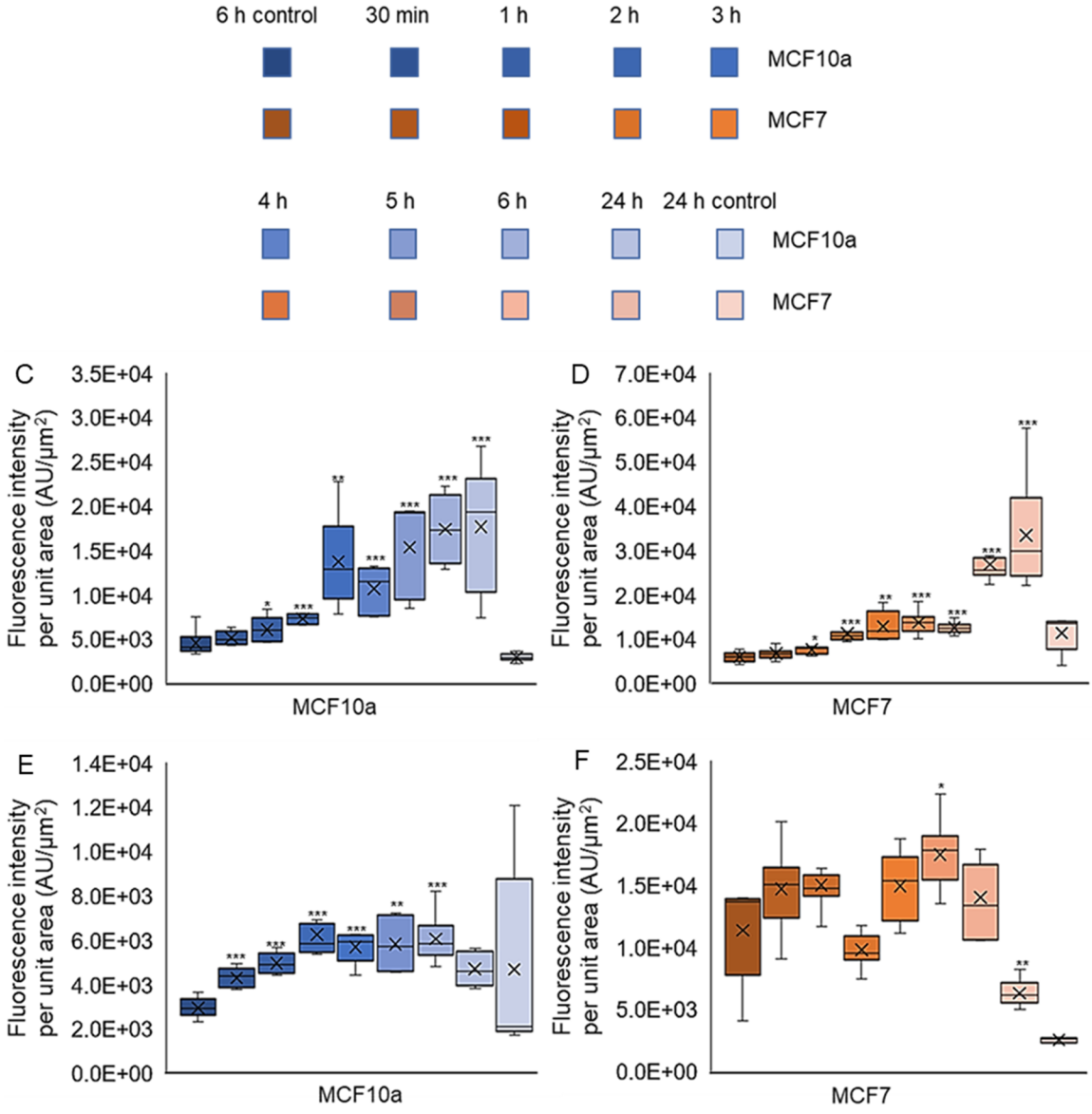

Figure 6. Continued.

mechanisms and nuclear import processes. Additionally, differences in nuclear pore complex composition or functionality and unique cellular stressors encountered by tumor cells may contribute to differences in CD nuclear translocation.

The concentration of CDs in the overall cell after exposure was higher than expected, indicating non-equilibrium conditions. CD uptake into the nucleus during the first 6 hours was nearly linear, suggesting a constant CD flux from the media into the cell. Compared to previous data, CDs were found to accumulate inside the nuclei and nuclear membrane, with 23.10% in MCF10a and 70.92% in MCF7 (calculated in the blue channel for 24 hours).

The kinetics of CD uptake, combined with cytoskeletal interactions, suggest that CDs interact with cytoskeletal proteins at the membrane before entering the cytosol via different mechanisms. Some CDs become entrapped in lysosomes while others penetrate the nuclear membrane. To explore the effect of cytoskeletal metabolomics on CD uptake to the nucleus, uptake studies were performed at 4 °C, pausing all energy-requiring mechanisms.

2.5. Cell paused CD uptake shows an early saturation like behavior

Lowering the cell temperature to 4 °C slows down most cellular metabolism and transport activities by reducing enzyme and transport protein activity. While complete cessation of these activities is not achievable, a considerable slowdown occurs, enhancing passive cell diffusion. In this state, active cytoskeleton-mediated transport activities do not interfere with CD diffusion

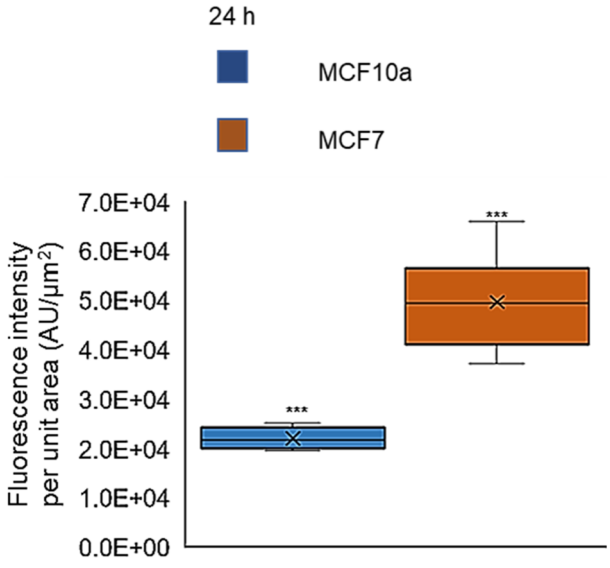

Figure 7. Nuclei isolated from cells show similar uptakes at 24 h in the blue channel (BP 420-480) for MCF10a (blue) and MCF7 (brown). Data are represented as a box and scatter plot with capper heads marking deviations, and boxes representing quartile range. Mean is represented as the Central solid line. *$p < 0.05$; **$p < 0.01$; ***$p < 0.001$ with respect to control.

(Aermes et al. 2021; Muratori, Pakhomov, and Pakhomova 2017; Naresh 2016; Reissis et al. 2013).

As reported in Figure 8, in MCF10a at 6 h as compared to normal uptake at 37 °C, the cells had 58.04% more CDs while the difference in CD uptake at 4 °C as compared to 37 °C in MCF7 at 4 h was non-significant. It was not feasible to measure CD uptake in MCF7 at 6 h as the MCF7 cells did not survive at that temperature for the given duration. At 4 °C, the amount of CDs isolated in the nucleus in MCF10a was 16.34% and in MCF7 was 92.62%, similar to the magnitudes observed at 37 °C discussed in the previous section.

Through a comprehensive literature review, we found studies on quantum dot diffusion in cells which explain this process. Quantum dots' diffusion constants at cell membranes increase when actin depolymerization occurs, possibly due to trapping within F-actin rich cellular cortexes at the inner face of plasma membranes (Svitkina 2020). Actin destabilization allows CDs to diffuse freely in the cytoplasm, resulting in two classes of uptake: slow diffusing and fast diffusing (Katrukha et al. 2017). While establishing the exact mechanism of uptake was beyond the scope of this work, we observed passive uptake up to saturation in metabolically paused cells and a constant flux in metabolically active cells. Even in paused cells, the concentration of CDs in the overall cell after exposure was higher than expected for equilibrium, indicating an affinity for or entrapment by intracellular moieties.

Given CDs' significant impact on various parameters including the cell cycle, which is epigenetically regulated by the nucleus, an effect on nuclear activity was anticipated. Small particles have been shown to trespass the nuclear membrane, with CDs of 2 nm exhibiting genotoxic effects in MCF7 cells and CdSe quantum dots of 5 nm showing genotoxicity in mice (Şimşek et al. 2020; Khalil et al. 2011).

2.6. CD uptake affects nuclear morphology

Once nuclear uptake of CDs was confirmed, we examined its impact on nuclear morphology. As already stated, the cytoskeleton influences the morphology of subcellular compartments, including the nucleus. Then, the effects induced by CDs to cytoskeleton structures can affect the nuclear morphology, explaining observed changes in cell division, which is epigenetically regulated. Nuclear morphology is critical for various cellular processes, including embryonic development, gene regulation, and cell motility. Altered nuclear morphology can hinder disease progression, affecting aspects such as cancer metastases and laminopathy (Fischer 2020; Heckenbach et al. 2022; Mounkes et al. 2003; Mukherjee, Chen, and Levy 2016).

To assess the effect on nuclear morphology, the nuclear membrane was stained with DRAQ-5 (Figure 9). Several parameters were investigated, including cell area, circularity, major axes, minor axes, aspect ratio and cell volume. Interestingly, most of the investigated parameters showed a significant change for both cell lines when exposed to CDs.

In MCF10a the circularity, area, minor axis and volume of cells was shown to increase by 34.62, 310.83, 67.84 and 40% respectively. The aspect ratio decreased by 7.77% (Supplementary Figure 12). In MCF7 the area, major axis, minor axis, aspect ratio, volume increased by 7.34, 6.03, 1.03, 4.41 and 52.52%. It is worth noting that, for most of these parameters, the cells were able to fully recover in the next 24 hours if no longer exposed to CDs. In light of previous observations, this change in morphology may be attributed to cytoskeletal reorganizations connected to the nucleus (Zhang, Alisafaei, et al. 2020). These parameters were also compared to morphological changes induced by destroying the cytoskeleton through Cytochalasin D (Supplementary Figure 13). These reorganizations could have led to morphological changes and structural alterations in subcellular organelles, potentially affecting their functionality (Glancy et al. 2020; van Zutphen, van der Klei, and Anal 2011). The subsequent recovery of

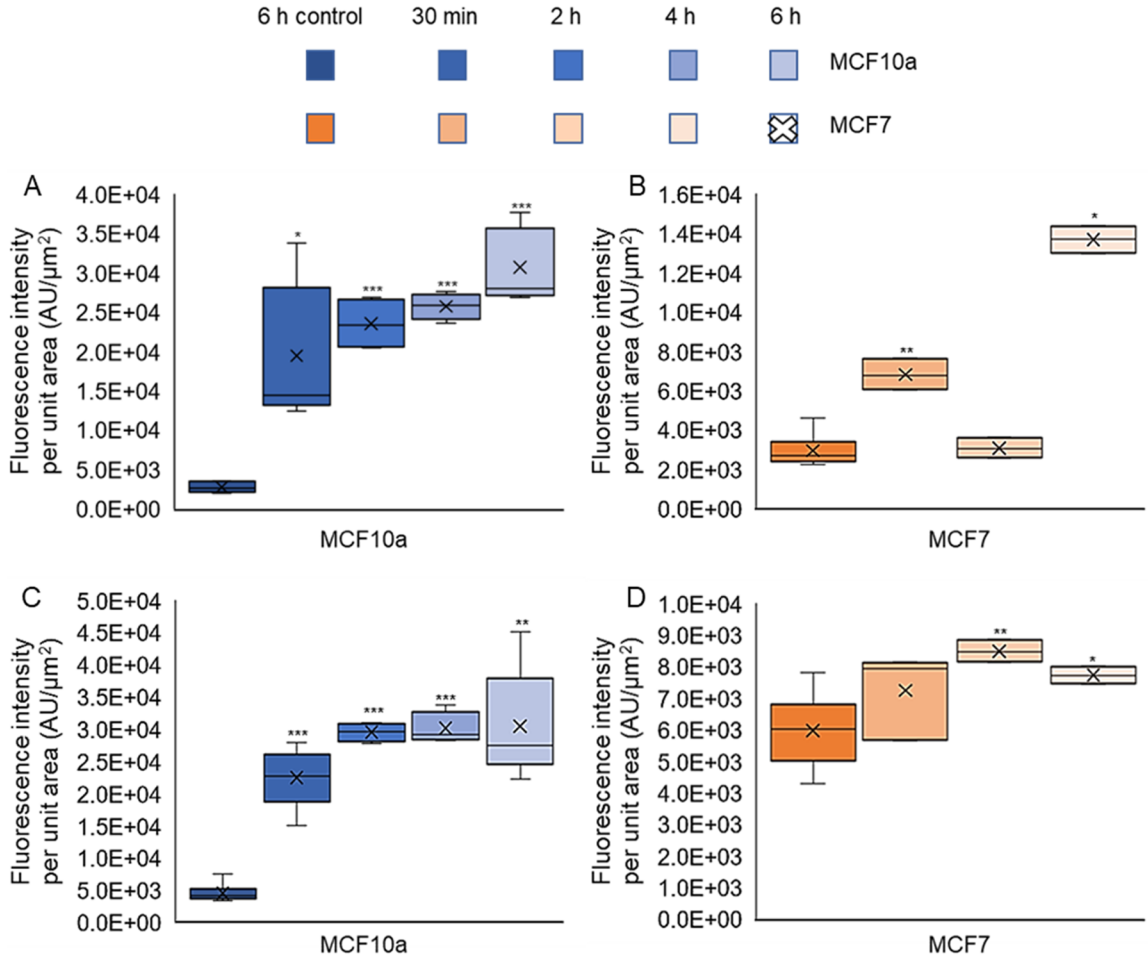

Figure 8. At 4 °C, CDs show a similar saturation like effect of 24 h in the blue channel (BP 420-480) for MCF10a (blue, A-cells and C-nucleus) and MCF7 (brown, A-cells and C-nucleus). Data are represented as a box and scatter plot with capper heads marking deviations, and boxes representing quartile range. Mean is represented as the Central solid line. *$p < 0.05$; **$p < 0.01$; ***$p < 0.001$ with respect to control.

these morphological parameters suggests that subcellular organizations may have been restored following the expulsion of internalized CDs.

2.7. CD uptake affects genotoxic chromatin condensation

In addition to the morphological impact of CDs on the nucleus, it is important to consider the potential for DNA damage. DNA damage can occur due to the direct presence and binding of small CDs to the genetic material or as a result of intermediate secretions of the cell in response to CDs exposure (e.g. ROS caused by oxidative stress) (Azzouz, Khan, and Palaniyar 2021; Kang et al. 2012; Salehi et al. 2018). In order to verify this hypothesis, analysis of the chromatin condensation state was conducted. Changes in chromatin condensation state can be correlated with either DNA damage or chromosome compaction during mitosis. Single and double stranded DNA was stained with TOPRO-3, and analyzed for differential chromatin condensations.

Interestingly, we observed an increase in the chromatin condensation in both cell lines. MCF7 chromosomes were nearly 32% more condensed upon exposure and MCF10a chromosomes showed 15% more condensation. As reported in the cell cycle analysis in our previous work, only 1.26% more cells were in the division phase in CD exposed MCF7 cells as compared to the unexposed cells. Since the change in chromatin condensation state found experimentally is significantly greater than the percentage of dividing cells, it is plausible that CDs and/or intermediate cell secretions also play a role (Kreuz and Fischle 2016). Overall, it is possible that the CDs have an impact in terms of DNA damage over 24 h. Since several anti-tumor therapies aim to target the DNA, these CDs can hence have a huge impact to develop as a nuclear-targeting therapy.

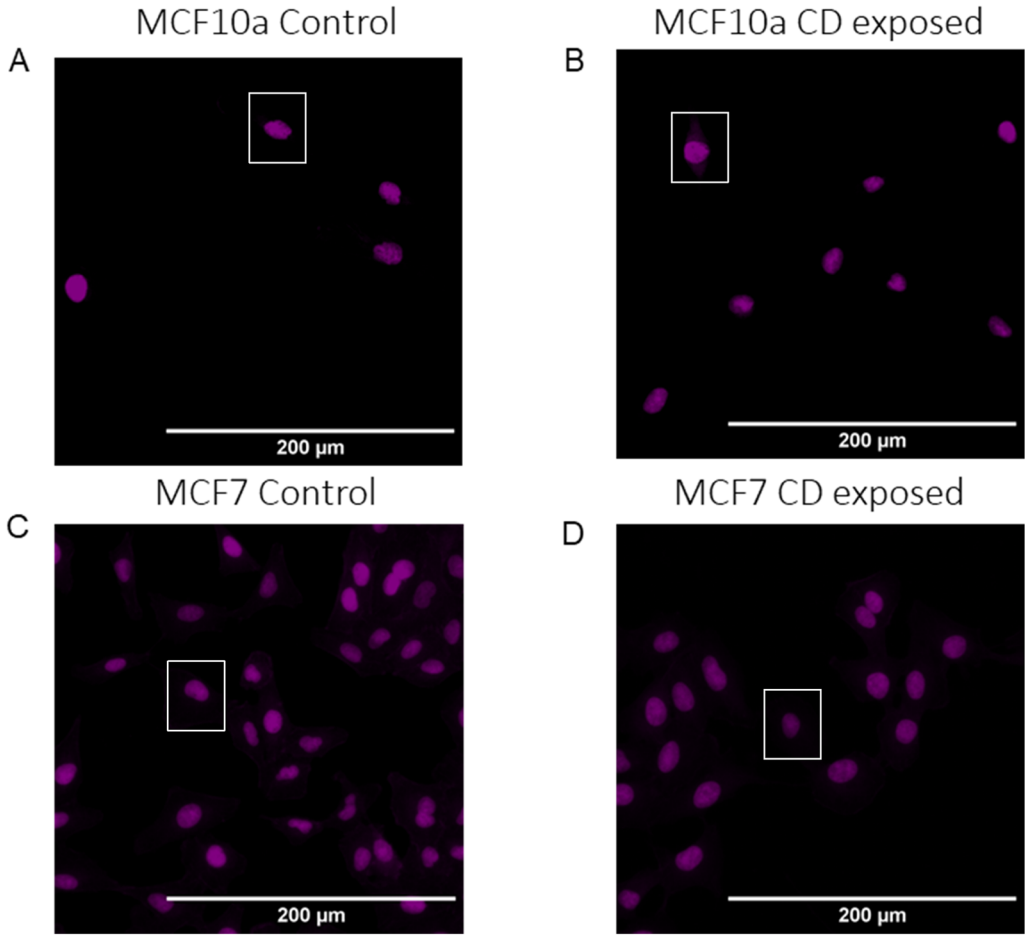

Figure 9. (A–D) MCF7 and MCF10a exhibit visible morphological changes in the nucleus (pink) when exposed to CDs for 24 h. Representative images of MCF7 and MCF10a nuclei stained with DRAQ-5 (and cells with WGA). Scale bar = 20 µm. (E–J) After 24 h of CD exposure, the cells show evident changes in morphology but also regain their original morphology after 24 h of recovery time. MCF10a cells (data in blue) show a significant decrease in their cell areas (top left), no significant change in circularity (top right), and a decreased aspect ratio after 24 h of CD exposure. However, all parameters completely recover after 24 h from exposure. Interestingly, the volume of MCF10a cells does not change after 24 h of exposure but significantly increases after an additional 24 h in CD-free media (bottom right), possibly indicating preparation for cell division. MCF7 cells (data in brown) show an initial decrease in area followed by recovery similar to MCF10a (top left), but exhibit a significant increase in circularity after 24 h of CD exposure, which is recovered after an additional 24 h in CD-free culture (top right). MCF7 shows no change in aspect ratio (bottom left) but shows an overall increase in cell volume after recovery, similar to MCF10a (bottom right). Graphs are represented as box plots with $n = 50$ cells across three samples, showing mean value, median, and interquartile range. p-Values indicated as $p < 0.05$, $p < 0.01$, and $p < 0.001$ with respect to negative controls.

Nucleus is the hub of gene expression and is responsible for key cellular processes, making it an attractive target for nanomedicine. Since these CDs have demonstrated the ability to enter the nucleus, they can be exploited for use in nuclear drug delivery and for their ability to cause disruptions to the nuclear structure. While gene delivery has been used to treat diseases like Parkinson's, immunodeficiency and genetic disorders, the traditional method of using adeno-associated virus (AAV) vectors are restricted by their small size capacity, immunogenicity, high production costs, invasive administration and inflammatory response (Puhl, D'Amato, and Gilbert 2019; Fischell and Fishman 2021). In contrast, non-viral vectors, with CDs being an example, are much more biocompatible, safer by being less toxic, cost-effective and tunable (Li and Huang 2000; Ren et al. 2021; Yin et al. 2014; Zu and Gao 2021). These combustion-generated CDs, with their ability to penetrate the nuclear membrane, represent a promising material nuclear drug delivery (Figure 10).

3. Conclusion

The use of small carbon nanomaterials and carbon quantum dots has emerged as a promising

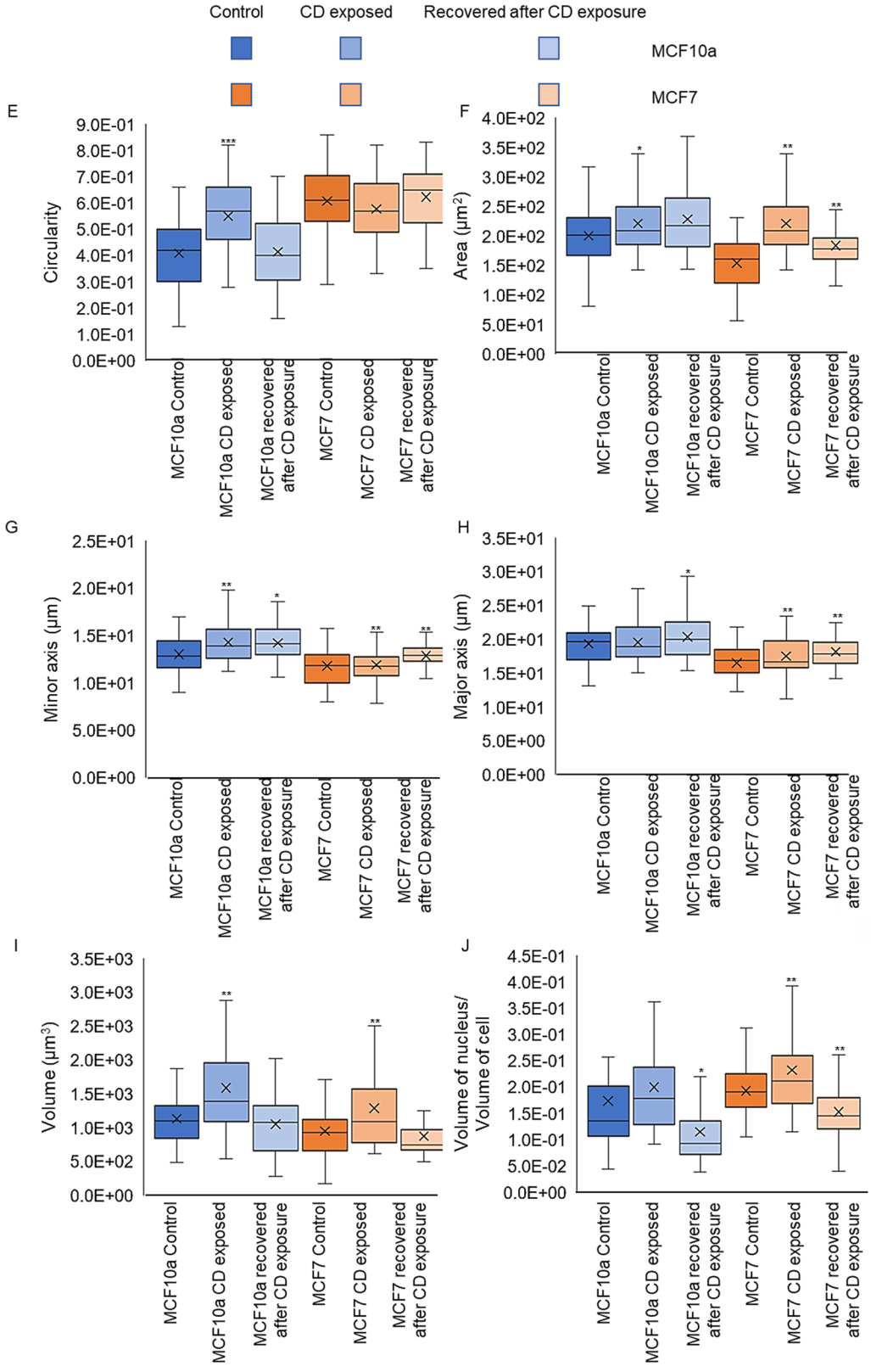

Figure 9. Continued.

technology for applications in the biomedical and chemical industries. Carbon nanodots, especially those on a small scale, gained attention in biomedicine due to their tunable optical properties and their ability to enter cells efficiently. Nevertheless, their application in the treatment of cancer and other human diseases has been hindered by a lack of comprehensive understanding

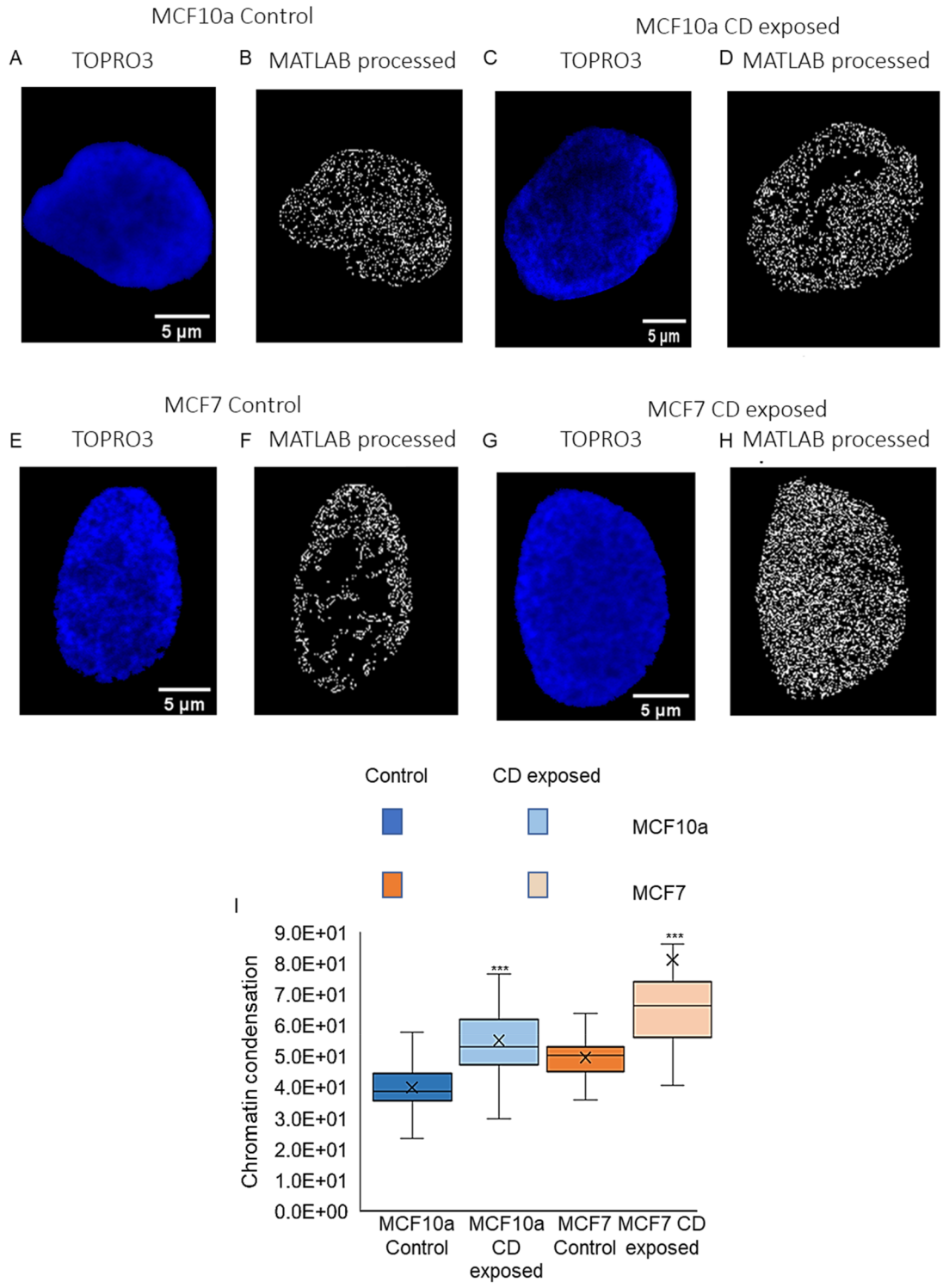

Figure 10. (A) Confocal imaging depicting the change in chromatin condensation state through TOPRO-3 staining. Scale bar = B: CD exposure increases chromatin condensation in MCF10a (blue) and MCF7 (brown). Data are represented as a box and scatter plot with capper heads marking deviations, and boxes representing quartile range. Mean is represented as the Central solid line. $p < 0.05$; $p < 0.01$; $p < 0.001$ with respect to control.

regarding the intracellular fate of these nanomaterials.

In this paper, we take advantage of recently developed fluorescing combustion-generated CDs to gain insights into the endocytic uptake including entry into the nucleus, at sub-lethal doses. Our findings reveal the presence of CDs in the nucleus of metabolically viable and metabolically frozen MCF7 breast

cancer cells and MCF10a breast epithelia. It is evident that these CDs have entered the cells causing damage to the actin, tubulin and paxillin moieties. Our results suggest that CDs are transported via both endocytosis-like pathways and passively, as indicated by a linear uptake in metabolically viable cells and non-metabolic uptakes at 4 °C, respectively. It is essential to highlight that CD uptake not only induced structural alterations in the cells by affecting protein intensities but has also had functional implications by impeding the migration of tumor cells. Such effects hold promises for targeted drug delivery and preferential cytotoxicity in cancer treatment, making carbon dots a potential candidate for anticancer therapy.

However, before these CDs can be used as nano-delivery systems, understanding their fate in the body is crucial for evaluating their potential. CDs, due to their small size and surface properties, can undergo rapid renal clearance, which may pose challenges for sustained delivery of therapeutic payloads. Renal filtration mechanisms can potentially lead to premature clearance of CDs from systemic circulation, limiting their residence time in target tissues. While renal filtration problems are recognized, addressing these challenges along with other *in vivo* challenges falls beyond the scope of the current paper. Future evaluations are warranted to comprehensively assess the biodistribution, pharmacokinetics, and potential renal toxicity of CDs before finally considering their clinical translation for therapeutic applications. Nonetheless, we believe that the unique physicochemical properties of CDs hold promise for alternative applications beyond traditional drug delivery systems. Further exploration and discussion of these potential novel applications are encouraged for future research endeavors.

4. Experimental methods

4.1. Nanoparticle synthesis and characterization

To achieve CD synthesis, a premixed laminar flat ethylene/air flame was stabilized in a McKenna burner. CDs were extracted from the overall particulate with organic solvents, producing an equivalence ratio of 2.46 of ethylene flames. Tuning the equivalence ratio produces fluorescent CDs from blue to yellow with different quantum yields allowing scalability.

CDs were collected and characterized as reported by Russo et al. (Russo et al. 2023) A brief summary is reported in this subsection. CD sampling was done by thermophoretic depositions on glass plates (75X25X1 mm^3) from end flame reactors (HAB = 15 nm). The plates were horizontally inserted into the flame for a short time of 2 s through an automated insertion procedure. The repetitions concluded after a total insertion time of 60 s, which was optimized to ensure enough material deposits of thin carbon films, avoiding experimental artifacts (Russo et al. 2023).

These glass plates which were covered by carbon materials were washed in dichloromethane to eradicate light molecular weight organic carbon. Insoluble carbon was removed from the plate by dispersion in ethanol in an ultrasonic bath (5 min, 59 kHz). This insoluble carbon was then filtered to separate the <20 nm fraction using an Anotop filter (Whatman). This fraction was then analyzed by absorption and fluorescence spectroscopy using analysis techniques reported in Sirignano et al. (Sirignano, Russo, and Ciajolo 2020).

For this paper, the CDs were retrieved by Size Exclusion Chromatography and had a mean size of 2 nm (range from 1 to 5 nm), reasonable spherical approximation and unitary density, as confirmed by ex situ on line analysis of particles size distribution. Particle on line analysis conducted with scanning mobility particle sizers showed a mode size of 2 nm, in agreement with *ex-situ* measurements. This size and amorphous characteristics were furtherly confirmed by transmission electron microscopy. Their stability was shown over 200 days and up to 80 °C, pH 8-10 (Conturso, Sirignano, and D'Anna 2017; Michelsen et al. 2020; Russo, D'Anna, et al. 2019; 2019; Sirignano, Russo, and Ciajolo 2020; Russo et al. 2023; Sirignano et al. 2017).

4.2. Cell culture

MCF10a cells (kindly donated by S. Piccolo, Istituto FIRC di Oncologia Molecolare, IFOM, Milan, Italy) were cultured in DMEM-F12 (Microgem) supplemented with 5% horse serum (ThermoScientific 16050122), 1% penicillin/streptomycin (Himedia), 1% L-glutamine (Himedia), 20 ng/ml Epidermal Growth Factor (EGF, Peprotech AF-100-5), 500 ng/ml human corticosteroids (Sigma-Aldrich H0396), and Insulin (Sigma-Aldrich I9278).

MCF7 cells were cultured in Minimum Essential Medium Eagle (MEM, Himedia) supplemented with 10% fetal bovine serum (F7524, Sigma-Aldrich), 1% penicillin/streptomycin (Himedia) and 1% L-glutamine.

4.3. Carbon dots exposure

MCF10a and MCF7 cells were seeded in glass bottom culture dishes (8 well-ibiTreat chamber slide 1 cm^2 per well, Ibidi, Germany) or in Wilco glass bottom well (35 mm with 22 mm aperture) at a density of 20,000 cells/cm^2. The next day cell media was replaced with media containing CDs at a concentration of 2.5E + 15 particles/ml until the planned time points. For observing cell recovery, cells were replaced with fresh media after washing the culture dish 3 times with 1X PBS (Microgem) to remove leftover CDs. The cells were allowed a recovery time of 24 h in fresh media before being processed for further analysis.

4.4. Analysis of cell migration

As described in Sections 2 and 3, MCF7 and MCF10a cells were seeded in Wilco glass bottom wells at a density of 10,000 cells/cm^2 (35 mm diameter and 22 mm aperture). 2 ml of CD containing media was added at the working concentration of 2.5E + 15 particles/ml for 24 h starting at the time of the first image acquisition. Cytochalasin D (30 µM in serum free media, ThermoScientific) and Nocodazole (15 µM in complete media, ThermoScientific) were added as positive controls in 2 different wells and exposed to cells for 30 min. The wells were then washed 3X with 1X PBS and then incubated with fresh cell media. Cell migration experiments were performed by time lapse microscopy using the TCS STED CW (Leica) equipped with a 10× air objective (NA = 0.22). Images were collected at 10 min intervals over ~23 h for both cell lines. Coordinate tracking was performed using FIJI's Manual Tracking plugin to trace an average of 50 cells per condition. The data was exported in an Excel sheet and analyzed using a downloadable open-source computer program DiPer to map the cell trajectories from the point of origin and calculate the average speed, mean square displacement (MSDs) and the chemotactic index. The α-values were calculated from the slope of log-log MSD curves (Gorelik and Gautreau 2014).

The velocity (v) was calculated as:

$$v = \frac{\Sigma\sqrt{(xi+1-xi)^2+(yi+1-yi)^2}}{n\cdot\Delta T} \quad (1)$$

MSD was calculated using the following formula by overlapping time intervals:

$$MSD(\tau) = \left[x(t-\tau)-x(t)\right]^2 + \left[y(t-\tau)-y(t)\right]^2 \quad (2)$$

The chemotactic index (CI) was calculated as:

$$CI = \frac{\sqrt{(xt-xi)^2+(yt-yi)^2}}{\Sigma\sqrt{(xi+1-xi)^2+(yi+1-yi)^2}} \quad (3)$$

Where x_i y_i are cell coordinates in the i^{th} time frame, ΔT is the time interval between two frames, n is the frame number, t is the time, τ is the lag time.

4.5. Immunostaining

After CD exposure as described in Section 3, the cell culture dishes were washed 3X with 1X PBS (Microgem) to remove any leftover media and then fixed with 4% paraformaldehyde (PFA, SigmaAldrich) for 20 min at room temperature. The dishes were washed again with 1X PBS and then the cells were permeabilized with 0.1% Saponin for 10 min followed by blocking with 2% BSA-PBS (Bovine Serum Albumin, SigmaAldrich). The cell culture dishes were stored in 1X PBS (Microgem) at 4 °C until further use.

4.5.1. Analysis of actin networks

To measure the effect of internalized CDs on F-actin, after 6 h and 24 h of CD exposure, the cells were fixed with 4% PFA (SigmaAldrich) for 20 min at room temperature followed by an incubation for 1.5 h with Phalloidin 647 (1:100, Phalloidin-iFluor 647 Reagent Abcam AB176759). The cells were washed 3X with 1X PBS and stored at 4 °C till imaging.

Images were acquired using a TCS STED CW (Leica) equipped with a 63× oil objective (NA = 1.4). equipped with confocal laser lines at excitation wavelengths of 405, 488 and 639 nm with respective filters at band pass 420–480 nm, band pass 505–530 nm and long pass 640–700 nm. The images were collected at 1 µm Z-spacing with a 1× zoom factor. For each time point and for each position, the fluorescent signal originating from the actin filaments (far red channel) were spatially masked to the signal derived from the CDs (blue and green channels) using ImageJ's JaCOP plugin (Lt 2006). The signals were thresholded uniformly in all channels and used to calculate the colocalization coefficients. Meander's overlap coefficients were calculated using ImageJ plugins (Manders, Verbeek, and Aten 1993). The results highlight the entrapment of CDs in MCF7 and MCF10a cells in actin filaments. M1 is the proportion of CD signal coincident with phalloidin signal over CD total intensity, while M2 quantifies the proportion of phalloidin

signal coincident with CD signal over phalloidin total intensity.

4.5.2. Analysis of β tubulin

To measure the effect of internalized CDs on β tubulin, after 24 h of CD exposure, the cells were fixed with 4% PFA (SigmaAldrich) for 20 min at room temperature followed by permeabilization with 0.1% Saponin (Sigma-Aldrich) solution for 10 min and blocking with 5% BSA (SigmaAldrich). The cells were stained with anti-β III tubulin antibody (1:400, Abcam AB78078) for 1 h at room temperature. Then, the cells were washed three times with 1X PBS and stained with donkey anti-mouse Alexa Fluor 555 (Abcam A150110) at 37 °C for 30 minutes. The cells were washed 3X with 1× PBS and stored at 4 °C till imaging.

Images were acquired using a confocal laser scanning microscope (LSM710 Zeiss Confocal) equipped with three diode laser lines (blue, $\lambda_{excitation}$ = 405 nm $\lambda_{emission}$ = 420–480 nm, and green channels, $\lambda_{excitation}$ = 488 nm $\lambda_{emission}$ = 505–530 nm, for CDs, red channel $\lambda_{excitation}$ = 555 nm, $\lambda_{emission}$ = 560–615 nm). The images were collected at 1 µm Z-spacing using a 63× plan apochromat oil immersion objective M27 (NA = 1.4) at an image resolution of 1024×1024 pixels (Saini et al. 2021) with a 1× zoom factor. For each time point and for each position, the fluorescent signal originating from the microtubule filaments (red channel) were spatially masked to the signal derived from the CDs (blue and green channels) using ImageJ's JaCOP plugin with uniform signal thresholding in all channels and to calculate the colocalization coefficients (Bolte and Cordelières 2006). Meander's overlap coefficients were calculated using ImageJ plugins (Manders, Verbeek, and Aten 1993). The results highlight the entrapment of CDs in MCF7 and MCF10a cells in microtubule filaments. M1 is the proportion of CD signal coincident with β-tubulin signal over CD total intensity, while M2 quantifies the proportion of β-tubulin signal coincident with CD signal over β-tubulin total intensity.

4.5.3. Analysis of nuclear morphology

As described in Section 5, cells were stained after 24 h CD exposure with DRAQ-5 fluorescent probe solution (5 mM, ThermoScientific, 1:1000) for 10 min and washed 3X with 1X PBS. Similarly, after 24 h recovery followed by 24 h exposure, cells were stained. The cells were imaged using confocal laser scanning microscope (LSM710 Zeiss Confocal) equipped with a confocal laser line at excitation wavelength of 555 nm and a band pass filter from 560 to 615 nm. The images were collected at 1 µm Z-spacing using a 63× plan apochromat oil immersion objective M27 (NA 1.4). Image resolution was 1024×1024 pixels (Saini et al. 2021) with a 1X zoom factor. For each condition, a minimum of 50 cells were analyzed with ImageJ built-in plugins to calculate the area, volume, and two morphological parameters, circularity (C) and aspect ratio (AR), defined as follows:

$$C = \frac{4\pi A}{P^2} \tag{4}$$

$$AR = \frac{major\,axis}{minor\,axis} \tag{5}$$

where A and P are the area and the perimeter of cells calculated by using the 'Measure' command in ImageJ, and major axis and minor axis are determined from the best-fitting ellipse in ImageJ. These parameters range from 1 to ∞, with 1 indicating an approximal circle in C and 0 indicating a straight line. These methods have been depicted in our previous papers (Panzetta, Verde, et al. 2020).

4.5.4. Analysis of focal adhesions

MCF10a and MCF7 cells were plated in a glass bottom petri as described in Section 3. After 24 h of CD exposure, the cells were washed 3X with 1X PBS, then fixed in 4% PFA for 20 min and washed 3X in 1X PBS. The cells were then permeabilized with 0.1% Saponin (Sigma-Aldrich) solution for 10 min and blocked with 5% BSA (SigmaAldrich). Afterwards, the cells were stained with anti-paxillin anti-rabbit primary antibody (1:200, Abcam AB32084) for 1.5 h at room temperature. Then, the cells were washed 3X with 1X PBS and stained with goat anti-rabbit 546 (1:400, Abcam A11035) for 1.5 h. Finally, cells were washed again with 1X PBS and stored in 1 ml 1X PBS per well at 4 °C. The images were analyzed using the LSM Zeiss Confocal microscope equipped with a 63X oil objective (NA = 1.4) and a pinhole-size of around 1 airy units (AU). Z stack images with 0.2 µm spacings were acquired with $\lambda_{excitation}$ = 534 nm and $\lambda_{emission}$ = 525 nm (with a 40 nm band-pass filter). Around 5 cells were imaged and analyzed using ImageJ. Paxillin stained images were filtered using median Gaussian filters with an average pixel size of 2.0. These images were subtracted from the original image using the image calculator tool and thresholded to remove single pixel noise. Close pixels were conjoint using the 'close'

command and analyzed. Morphological parameters of FACs were quantified and plotted against time.

4.5.5. Analysis of chromatin condensation

Fixed and permeabilized cells as described in Section 5 were blocked using 5% BSA (SigmaAldrich) and then stained for 20 min using 1:1000 TOPRO3 (Invitrogen) far red dye. The nucleus was imaged using the TCS STED CW (Leica) equipped with a 63X/0.8 M27 oil objective (NA = 1.4) and analyzed to calculate the edge density (number of edges/area of nucleus) of the chromosomes. The images were converted to 8-bit grayscale and analyzed using MATLAB. The MATLAB routine processed 8-bit grayscale raw images to detect their Sobel edges to identify the nucleus. Using the same MATLAB routine, the results were thresholded to separate extensively condensed chromatin from minimally condensed chromatin by calculating their intensity. The nuclear outline was removed and the total number of chromatin edges per unit nuclear area was calculated. Extensively condensed chromatin structures had a higher edge density than minimally condensed chromatin structures. This routine was published by Irianto et al. (Irianto, Lee, and Knight 2014)

4.6. Quantification of CD uptake

Cells were cultured as described in Sections 2 and 3 in a 8 well-ibiTreat chamber slide (1 cm^2 per well, Ibidi, Germany). At the planned timepoints (30 min, 1 h, 2 h, 3 h, 4 h, 6 h) CD containing cell media was replaced with fresh media. In another 8 well-ibiTreat chamber slide, the cells were exposed to 24 h of CD exposure. The µ-slides were washed 3X with 1X PBS (Microgem) and fixed using 4% Paraformaldehyde (PFA, Sigma Aldrich) for 20 min at room temperature and washed with 1X Hank's balanced salt solution (HBSS, MicroGem). The cell membranes were then stained with Wheat Germ Agglutinin (WGA)-Alexa Fluor 555 conjugate solution (ThermoScientific, 1:500 dilution) and DRAQ-5 fluorescent probe solution (5 mM, ThermoScientific, 1:1000) for 10 min and washed 3X with 1X PBS. The cells were stored at 4 °C until imaging. Images were acquired using Z-spacings of 1 µm to cover the total cell volume. The imaging was done using a confocal laser scanning microscope (LSM710 Zeiss Confocal) equipped with four diode laser lines (blue, $\lambda_{excitation}$ = 405 nm $\lambda_{emission}$ = 420–480 nm, and green channels, $\lambda_{excitation}$ = 488 nm $\lambda_{emission}$ = 505–530 nm, for CDs, red channel $\lambda_{excitation}$ = 555 nm, $\lambda_{emission}$ = 560–615 nm for cell membranes, far-red channel $\lambda_{excitation}$ = 639 nm, $\lambda_{emission}$ = 640–700 nm for nuclear membranes), using a 63X oil immersion objective (NA = 1.4). For each time-point, an average of five positions (one to three cells for each position) were imaged. The sum of the projection intensities of all focal planes were calculated using Fiji ImageJ (NIH software) for both blue and green color channels. CD internalization at each time-point was evaluated by calculating the integrated fluorescence intensity within individual cell and nuclear boundaries of the projected sum intensity. Red channel (WGA) images were used to extract individual cell borders and volume and far red (DRAQ-5) images were used to calculate nuclear borders and volume. The volume was calculated by ImageJ's Voxel Counter plugin. Data was plotted against time by calculating the integrated fluorescence intensity normalized with the corresponding cell volume or nuclear area.

4.7. Analysis of cell paused CD uptake

After 24 h of CD exposure as described in Section 3, the cells were paused to stop all metabolic activity by keeping them at 4 °C for 30 min. The cell membranes were then stained with Wheat Germ Agglutinin (WGA)-Alexa Fluor 555 conjugate solution (ThermoScientific, 1:500 dilution) and DRAQ-5 fluorescent probe solution (5 mM, ThermoScientific, 1:1000) for 10 min in cell media and washed 3X with 1X PBS. The wells were replaced with normal media. Images were acquired using a confocal laser scanning microscope (LSM710 Zeiss Confocal) as described in Section 6, using a 63X oil immersion objective (NA = 1.4). For each time-point, an average of two to three positions (one to three cells for each position) were imaged. Data was plotted against time by calculating the integrated fluorescence intensity normalized with the corresponding cell volume.

4.8. Isolation of nuclei

MCF10a and MCF7 cells were grown in T-25 flasks at a density of 20,000 cells/cm^2. Cells were incubated with 7 ml of CD containing media as described in Section 3. After trypsinization, the cells were collected in 15 ml conical tubes and centrifuged at 11,000 rpm for 5 min at 4 °C. The supernatant was discarded and 2 ml of nuclei extraction buffer (320 mM Sucrose (SigmaAldrich), 5 mM MgCl2 (SigmaAldrich), 10 mM HEPES (SigmaAldrich) and 1% Triton (SigmaAldrich)) was added to the pellet and vortexed gently. MCF10a cells were incubated for 5 min and MCF7 cells were

incubated for 10 min at 4 °C and then centrifuged at 2000 g for 5 min at 4 °C. The supernatant was discarded and the pellet was washed in nuclei of storage buffer (320 mM Sucrose (SigmaAldrich), 5 mM MgCl2 (SigmaAldrich), 10 mM HEPES (SigmaAldrich)). The pellet was then resuspended in 2 ml of nuclei storage buffer and pipetted to avoid clumps. The isolated nuclei were stored at −80 °C until further use. The uptake into these nuclei were then quantified in single Z planes as described in Section 6.

4.9. Quantifying membrane uptake

The cells were grown as described in Section 2 in 35 mm dishes and incubated with CDs as described in Section 3. After 24 h of exposure, the cells were scraped using a cell scraper (ThermoScientific) and imaged using the confocal laser scanning microscope (LSM710 Zeiss Confocal) as discussed in Section 6. For each time point, around 20 cells were imaged. Using ImageJ, the integrated fluorescence intensity of individual cell membranes were calculated. Red channel (WGA stained) images were used to extract individual cell borders. Data was plotted against time by calculating the integrated fluorescence intensity normalized with the corresponding membrane area.

4.10. Statistical analysis

Data are reported as mean ± standard error of the mean (SEM), unless otherwise indicated. All statistical comparisons are performed with Student's unpaired test. *p*-values of <0.05 indicate a statistically significant difference.

All necessary figures are included to provide comprehensive support for the main text. Hour-wise data of migration studies, alternative luminescent channels for carbon dots, etc. are present in the supplementary file to support the understanding of the figures in the main text.

Author contributions

The manuscript was written through contributions of all authors. All authors have given approval to the final version of the manuscript.

Disclosure statement

No potential conflict of interest was reported by the author(s).

Funding

We acknowledge financial support under the National Recovery and Resilience Plan (NRRP), Mission 4, Component 2, Investment 1.1, Call for tender No. 1409 published on 14.9.2022 by the Italian Ministry of University and Research (MUR), funded by the European Union – NextGenerationEU– Project Title Production of sustainable carbon dots for cell diagnostics and targeting (POLLINATE) – CUP E53D23017250001- Grant Assignment Decree No. 1385 adopted on 01/09/23 by the Italian Ministry of Ministry of University and Research (MUR).

ORCID

Nikita Dinger http://orcid.org/0000-0001-6478-0892
Carmela Russo http://orcid.org/0000-0002-6891-4250
Sabato Fusco http://orcid.org/0000-0001-7999-8640
Paolo A. Netti http://orcid.org/0000-0002-2435-7181
Mariano Sirignano http://orcid.org/0000-0003-4363-7194
Valeria Panzetta http://orcid.org/0000-0001-6174-4116

Data availability statement

The data that support the findings of this study are available from the corresponding author upon reasonable request.

References

Abuetabh, Y., H. H. Wu, C. Chai, H. Al Yousef, S. Persad, C. M. Sergi, and R. Leng. 2022. "DNA Damage Response Revisited: The p53 Family and Its Regulators Provide Endless Cancer Therapy Opportunities." *Experimental & Molecular Medicine* 54 (10): 1658–1669. https://doi.org/10.1038/s12276-022-00863-4.

Aermes, C., A. Hayn, T. Fischer, and C. T. Mierke. 2021. "Cell Mechanical Properties of Human Breast Carcinoma Cells Depend on Temperature." *Scientific Reports* 11 (1): 10771. https://doi.org/10.1038/s41598-021-90173-y.

Agostinetto, E., J. Gligorov, and M. Piccart. 2022. "Systemic Therapy for Early-Stage Breast Cancer: learning from the past to Build the Future." *Nature Reviews-Clinical Oncology* 19 (12): 763–774. https://doi.org/10.1038/s41571-022-00687-1.

Ahlinder, L., B. Ekstrand-Hammarström, P. Geladi, and L. Osterlund. 2013. "Large Uptake of Titania and Iron Oxide Nanoparticles in the Nucleus of Lung Epithelial Cells as Measured by Raman Imaging and Multivariate Classification." *Biophysical Journal* 105 (2): 310–319. https://doi.org/10.1016/j.bpj.2013.06.017.

Alexandrova, A., and M. Lomakina. 2022. "How Does Plasticity of Migration Help Tumor Cells to Avoid Treatment: Cytoskeletal Regulators and Potential Markers." *Frontiers in Pharmacology* 13: 962652. https://doi.org/10.3389/fphar.2022.962652.

Ali, M. R. K., Y. Wu, D. Ghosh, B. H. Do, K. Chen, M. R. Dawson, N. Fang, T. A. Sulchek, and M. A. El-Sayed. 2017. "Nuclear Membrane-Targeted Gold Nanoparticles Inhibit Cancer Cell Migration and Invasion." *ACS Nano*. 11 (4): 3716–3726. https://doi.org/10.1021/acsnano.6b08345.

Azzouz, D., M. A. Khan, and N. Palaniyar. 2021. "ROS Induces NETosis by Oxidizing DNA and Initiating DNA Repair." *Cell Death Discovery*. 7 (1): 113. https://doi.org/10.1038/s41420-021-00491-3.

Barhoum, A., M. L. García-Betancourt, J. Jeevanandam, E. A. Hussien, S. A. Mekkawy, M. Mostafa, M. M. Omran, M. S. Abdalla, and M. Bechelany. 2022. "Review on Natural,

Incidental, Bioinspired, and Engineered Nanomaterials: History, Definitions, Classifications, Synthesis, Properties, Market, Toxicities, Risks, and Regulations." *Nanomaterials* 12 (2):177. https://doi.org/10.3390/nano12020177.

Barooji, Y. F., K. G. Hvid, I. I. Petitjean, J. M. Brickman, L. B. Oddershede, and P. M. Bendix. 2021. "Changes in Cell Morphology and Actin Organization in Embryonic Stem Cells Cultured under Different Conditions." *Cells* 10(11): 2859. https://doi.org/10.3390/cells10112859.

Behzadi, S., V. Serpooshan, W. Tao, M. A. Hamaly, M. Y. Alkawareek, E. C. Dreaden, D. Brown, A. M. Alkilany, O. C. Farokhzad, and M. Mahmoudi. 2017. "Cellular Uptake of Nanoparticles: journey inside the Cell." *Chemical Society Reviews* 46 (14): 4218–4244. https://doi.org/10.1039/c6cs00636a.

Biswas, M. C., M. T. Islam, P. K. Nandy, and M. M. Hossain. 2021. "Graphene Quantum Dots (GQDs) for Bioimaging and Drug Delivery Applications: A Review." *ACS Materials Letters*. 3: 889.

Blajeski, A. L., V. A. Phan, T. J. Kottke, and S. H. Kaufmann. 2002. "G(1) and G(2) Cell-Cycle Arrest following Microtubule Depolymerization in Human Breast Cancer Cells." *The Journal of Clinical Investigation* 110 (1): 91–99. https://doi.org/10.1172/JCI200213275.

Bolte, S., and F. P. Cordelières. 2006. "A Guided Tour into Subcellular Colocalization Analysis in Light Microscopy." *Journal of Microscopy*. 224: 213.

Burridge, K. 2017. "Focal Adhesions: A Personal Perspective on a Half Century of Progress." *The FEBS Journal* 284 (20): 3355–3361. https://doi.org/10.1111/febs.14195.

Carneiro, B. A., and W. S. El-Deiry. 2020. "Targeting Apoptosis in Cancer Therapy." *Nature Reviews. Clinical Oncology* 17 (7): 395–417. https://doi.org/10.1038/s41571-020-0341-y.

Chen, J., D. Yan, and Y. Chen. 2023. "Understanding the Driving Force for Cell Migration Plasticity." *Biophysical Journal* 122 (18): 3570–3576. https://doi.org/10.1016/j.bpj.2023.04.008.

Cheng, J., K. A. S. Fernando, L. M. Veca, Y.-P. Sun, A. I. Lamond, Y. W. Lam, and S. H. Cheng. 2008. "Reversible Accumulation of PEGylated Single-Walled Carbon Nanotubes in the Mammalian Nucleus." *ACS Nano*. 2 (10): 2085–2094. https://doi.org/10.1021/nn800461u.

Chittasupho, C., A. Manthaisong, S. Okonogi, S. Tadtong, and W. Samee. 2021. "Effects of Quercetin and Curcumin Combination on Antibacterial, Antioxidant, *In Vitro* Wound Healing and Migration of Human Dermal Fibroblast Cells." *International Journal of Molecular Sciences* 23(1): 142. https://doi.org/10.3390/ijms23010142.

Conturso, M., M. Sirignano, and A. D'Anna. 2017. "Effect of 2,5-Dimethylfuran Doping on Particle Size Distributions Measured in Premixed Ethylene/Air Flames." *Proceedings of the Combustion Institute*. 36: 985.

Davidson, P. M., and B. Cadot. 2021. "Actin On and Around the Nucleus." *Trends in Cell Biology* 31 (3): 211–223. https://doi.org/10.1016/j.tcb.2020.11.009.

Saini, D., G. Kumar, J. Kaushik, R. Aggarwal, K. Tripathi, and S. Sonkar. 2021. "Carbon Nanomaterials Derived from Black Carbon Soot: A Review of Materials and Applications." *ACS Applied Nano Materials* 4(12): 12825–12844. https://doi.org/10.1021/acsanm.1c02840.

Desai, N. 2012. "Challenges in Development of Nanoparticle-Based Therapeutics." *The AAPS Journal* 14 (2): 282–295. https://doi.org/10.1208/s12248-012-9339-4.

Dinger, N., V. Panzetta, C. Russo, P. A. Netti, and M. Sirignano. 2022. "*In Vitro* Effects of Combustion Generated Carbon Dots on Cellular Parameters in Healthy and Cancerous Breast Cells." *Nanotoxicology* 16 (6–8): 733–756. https://doi.org/10.1080/17435390.2022.2144775.

Elkin, S. R., A. M. Lakoduk, and S. L. Schmid. 2016. "Endocytic Pathways and Endosomal Trafficking: A Primer." *Wiener Medizinische Wochenschrift* 166 (7–8): 196–204. https://doi.org/10.1007/s10354-016-0432-7.

Fahrenkrog, B., and U. Aebi. 2003. "The Nuclear Pore Complex: Nucleocytoplasmic Transport and Beyond." *Nature Reviews Molecular Cell Biology*. 4: 757.

Fischell, J. M., and P. S. Fishman. 2021. "A Multifaceted Approach to Optimizing AAV Delivery to the Brain for the Treatment of Neurodegenerative Diseases." *Frontiers in Neuroscience* 15 (747726). https://doi.org/10.3389/fnins.2021.747726.

Fischer, E. G. 2020. "Nuclear Morphology and the Biology of Cancer Cells." *Acta Cytologica* 64 (6): 511–519. https://doi.org/10.1159/000508780.

Fletcher, D. A., and R. D. Mullins. 2010. "Cell Mechanics and the Cytoskeleton." *Nature* 463 (7280): 485–492. https://doi.org/10.1038/nature08908.

Fu, X., Y. Shi, T. Qi, S. Qiu, Y. Huang, X. Zhao, Q. Sun, and G. Lin. 2020. "Diagnostic and Therapeutic Approaches for Glioblastoma and Neuroblastoma Cancers Using Chlorotoxin Nanoparticles." *Signal Transduction and Targeted Therapy* 5: 262.

Gallaher, J. A., J. S. Brown, and A. R. A. Anderson. 2019. "The Impact of Proliferation-Migration Tradeoffs on Phenotypic Evolution in Cancer." *Scientific Reports* 9 (1): 2425. https://doi.org/10.1038/s41598-019-39636-x.

Geiger, B., J. P. Spatz, and A. D. Bershadsky. 2009. "Environmental Sensing Through Focal Adhesions." *Nature Reviews Molecular Cell Biology*. 10: 21.

Geltmeier, A., B. Rinner, D. Bade, K. Meditz, R. Witt, U. Bicker, C. Bludszuweit-Philipp, and P. Maier. 2015. "Characterization of Dynamic Behaviour of MCF7 and MCF10A Cells in Ultrasonic Field Using Modal and Harmonic Analyses." *PLOS One*. 10 (8): e0134999. https://doi.org/10.1371/journal.pone.0134999.

Glancy, B., Y. Kim, P. Katti, and T. B. Willingham. 2020. "The Functional Impact of Mitochondrial Structure Across Subcellular Scales." *Frontiers in Physiology* 11: 541040. https://doi.org/10.3389/fphys.2020.541040.

Gonciar, D., T. Mocan, C. T. Matea, C. Zdrehus, O. Mosteanu, L. Mocan, and T. Pop. 2019. "Nanotechnology in Metastatic Cancer Treatment: Current Achievements and Future Research Trends." *Journal of Cancer* 10 (6): 1358–1369. https://doi.org/10.7150/jca.28394.

Gorelik, R., and A. Gautreau. 2014. "Quantitative and Unbiased Analysis of Directional Persistence in Cell Migration." *Nature Protocols* 9 (8): 1931–1943. https://doi.org/10.1038/nprot.2014.131.

Grady, M. E., E. Parrish, M. A. Caporizzo, S. C. Seeger, R. J. Composto, and D. M. Eckmann. 2017. "Intracellular Nanoparticle Dynamics Affected by Cytoskeletal Integrity." *Soft Matter* 13 (9): 1873–1880. https://doi.org/10.1039/c6sm02464e.

Guo, D., J. H. Lei, D. Rong, T. Zhang, B. Zhang, Z. Tang, H.-M. Shen, C.-X. Deng, and S. Qu. 2022. "Photocatalytic Pt(IV)-Coordinated Carbon Dots for Precision Tumor Therapy." *Advanced Science* 9: 2205106.

Gupton, S. L., and C. M. Waterman-Storer. 2006. "Spatiotemporal Feedback between Actomyosin and Focal-Adhesion Systems Optimizes Rapid Cell Migration." *Cell* 125 (7): 1361–1374. https://doi.org/10.1016/j.cell.2006.05.029.

Heckenbach, I., G. V. Mkrtchyan, M. B. Ezra, D. Bakula, J. S. Madsen, M. H. Nielsen, D. Oró, et al. 2022. "Nuclear Morphology is a Deep Learning Biomarker of Cellular Senescence." *Nature Aging* 2 (8): 742–755. https://doi.org/10.1038/s43587-022-00263-3.

Hinshaw, J. E., B. O. Carragher, and R. A. Milligan. 1992. "Architecture and Design of the Nuclear Pore Complex." *Cell* 69 (7): 1133–1141. https://doi.org/10.1016/0092-8674(92)90635-p.

Hu, Y., M. L. Becker, and R. K. Willits. 2023. "Quantification of Cell Migration: Metrics Selection to Model Application." *Frontiers in Cell and Developmental Biology* 11: 1155882.

Huang, R., and P.-K. Zhou. 2021. "DNA Damage Repair: Historical Perspectives, Mechanistic Pathways and Clinical Translation for Targeted Cancer Therapy." *Signal Transduction and Targeted Therapy* 6: 254.

Huo, S., S. Jin, X. Ma, X. Xue, K. Yang, A. Kumar, P. C. Wang, J. Zhang, Z. Hu, and X.-J. Liang. 2014. "Ultrasmall Gold Nanoparticles as Carriers for Nucleus-Based Gene Therapy Due to Size-Dependent Nuclear Entry." *ACS Nano* 8 (6): 5852–5862. https://doi.org/10.1021/nn5008572.

Irianto, J., D. A. Lee, and M. M. Knight. 2014. "Quantification of Chromatin Condensation Level by Image Processing." *Medical Engineering & Physics* 36 (3): 412–417. https://doi.org/10.1016/j.medengphy.2013.09.006.

JayaNandanan, N., R. Mathew, and M. Leptin. 2014. "Guidance of Subcellular Tubulogenesis by Actin under the Control of a Synaptotagmin-like Protein and Moesin." *Nature Communications* 5: 3036. https://doi.org/10.1038/ncomms4036.

Ji, C., Y. Zhou, R. M. Leblanc, and Z. Peng. 2020. "Recent Developments of Carbon Dots in Biosensing: A Review." *ACS Sensors* 5 (9): 2724–2741. https://doi.org/10.1021/acssensors.0c01556.

Kang, B., M. A. Mackey, and M. A. El-Sayed. 2010. "Nuclear Targeting of Gold Nanoparticles in Cancer Cells Induces DNA Damage, Causing Cytokinesis Arrest and Apoptosis." *Journal of the American Chemical Society* 132 (5): 1517–1519. https://doi.org/10.1021/ja9102698.

Kang, M. A., E.-Y. So, A. L. Simons, D. R. Spitz, and T. Ouchi. 2012. "DNA Damage Induces Reactive Oxygen Species Generation through the H2AX-Nox1/Rac1 Pathway." *Cell Death & Disease* 3 (1): e249–e249. https://doi.org/10.1038/cddis.2011.134.

Kasza, K. E., and J. A. Zallen. 2011. "Dynamics and Regulation of Contractile Actin-Myosin Networks in Morphogenesis." *Current Opinion in Cell Biology*. 23: 30.

Katrukha, E. A., M. Mikhaylova, H. X. van Brakel, P. M. van Bergen En Henegouwen, A. Akhmanova, C. C. Hoogenraad, and L. C. Kapitein. 2017. "Probing Cytoskeletal Modulation of Passive and Active Intracellular Dynamics Using Nanobody-Functionalized Quantum Dots." *Nature Communications* 8: 14772. https://doi.org/10.1038/ncomms14772.

Kaverina, I., and A. Straube. 2011. "Regulation of Cell Migration by Dynamic Microtubules." *Seminars in Cell & Developmental Biology*. 22: 968.

Khalil, W. K. B., E. Girgis, A. N. Emam, M. B. Mohamed, and K. V. Rao. 2011. "Genotoxicity Evaluation of Nanomaterials: dna Damage, Micronuclei, and 8-Hydroxy-2-Deoxyguanosine Induced by Magnetic Doped CdSe Quantum Dots in Male Mice." *Chemical Research in Toxicology* 24 (5): 640–650. https://doi.org/10.1021/tx2000015.

Kim, S., and P. A. Coulombe. 2010. "Emerging Role for the Cytoskeleton as an Organizer and Regulator of Translation." *Nature Reviews Molecular Cell Biology*. 11: 75.

Kour, R., S. Arya, S.-J. Young, V. Gupta, P. Bandhoria, and A. Khosla. 2020. "Review—Recent Advances in Carbon Nanomaterials as Electrochemical Biosensors." *Journal of The Electrochemical Society* 167 (3): 037555. https://doi.org/10.1149/1945-7111/ab6bc4.

Kreuz, S., and W. Fischle. 2016. "Oxidative Stress Signaling to Chromatin in Health and Disease." *Epigenomics* 8 (6): 843–862. https://doi.org/10.2217/epi-2016-0002.

Latha, B. D., K. Soumya, N. More, C. Mounika, A. T. Guduru, G. Singh, and G. Kapusetti. 2023. "Fluorescent Carbon Quantum Dots for Effective Tumor Diagnosis: A Comprehensive Review." *Biomedical Engineering Advances* 5: 100072.

Lee, M.-H., P.-H. Wu, J. R. Staunton, R. Ros, G. D. Longmore, and D. Wirtz. 2012. "Mismatch in Mechanical and Adhesive Properties Induces Pulsating Cancer Cell Migration in Epithelial Monolayer." *Biophysical Journal* 102 (12): 2731–2741. https://doi.org/10.1016/j.bpj.2012.05.005.

Lee, S. W. L., C. Paoletti, M. Campisi, T. Osaki, G. Adriani, R. D. Kamm, C. Mattu, and V. Chiono. 2019. "MicroRNA Delivery Through Nanoparticles." *Journal of Controlled Release*. 313: 80.

Li, S., and L. Huang. 2000. "Nonviral Gene Therapy: promises and Challenges." *Gene Therapy* 7 (1): 31–34. https://doi.org/10.1038/sj.gt.3301110.

Liu, Z., K. Chen, C. Davis, S. Sherlock, Q. Cao, X. Chen, and H. Dai. 2008. "Drug Delivery with Carbon Nanotubes for *in Vivo* Cancer Treatment." *Cancer Research* 68 (16): 6652–6660. https://doi.org/10.1158/0008-5472.CAN-08-1468.

Liu, Z., S. J. Lee, S. Park, K. Konstantopoulos, K. Glunde, Y. Chen, and I. Barman. 2020. "Cancer Cells Display Increased Migration and Deformability in Pace with Metastatic Progression." *FASEB Journal* 34 (7): 9307–9315. https://doi.org/10.1096/fj.202000101RR.

Manders, E. M. M., F. J. Verbeek, and J. A. Aten. 1993. "Measurement of Co-Localization of Objects in Dual-Colour Confocal Images." *Journal of Microscopy*. 169: 375.

Melzer, C., J. von der Ohe, and R. Hass. 2019. "Involvement of Actin Cytoskeletal Components in Breast Cancer Cell Fusion with Human Mesenchymal Stroma/Stem-Like Cells." *International Journal of Molecular Sciences* 20 (4): 876. https://doi.org/10.3390/ijms20040876.

Michelsen, H. A., M. B. Colket, P.-E. Bengtsson, A. D'Anna, P. Desgroux, B. S. Haynes, J. H. Miller, G. J. Nathan, H. Pitsch, and H. Wang. 2020. "A Review of Terminology Used to Describe Soot Formation and Evolution under Combustion and Pyrolytic Conditions." *ACS Nano*. 14 (10): 12470–12490. https://doi.org/10.1021/acsnano.0c06226.

Mitchell, M. J., M. M. Billingsley, R. M. Haley, M. E. Wechsler, N. A. Peppas, and R. Langer. 2021. "Engineering Precision Nanoparticles for Drug Delivery." *Nature Reviews Drug Discovery* 20: 101.

Mounkes, L., S. Kozlov, B. Burke, and C. L. Stewart. 2003. "The Laminopathies: nuclear Structure Meets Disease." *Current Opinion in Genetics & Development* 13 (3): 223–230. https://doi.org/10.1016/s0959-437x(03)00058-3.

Mukherjee, R. N., P. Chen, and D. L. Levy. 2016. "Recent Advances in Understanding Nuclear Size and Shape." *Nucleus* 7: 167.

Muratori, C., A. G. Pakhomov, and O. N. Pakhomova. 2017. "Effect of Cooling on Cell Volume and Viability After Nanoelectroporation." *Journal of Membrane Biology*. 250: 217.

Murciano-Goroff, Y. R., B. S. Taylor, D. M. Hyman, and A. M. Schram. 2020. "Toward a More Precise Future for Oncology." *Cancer Cell* 37 (4): 431–442. https://doi.org/10.1016/j.ccell.2020.03.014.

Naik, K., S. Chaudhary, L. Ye, and A. S. Parmar. 2022. "A Strategic Review on Carbon Quantum Dots for Cancer-Diagnostics and Treatment." *Frontiers in Bioengineering and Biotechnology* 10: 882100. https://doi.org/10.3389/fbioe.2022.882100.

Nakaseko, Y., and M. Yanagida. 2001. "Cell Biology. Cytoskeleton in the Cell Cycle." *Nature* 412 (6844): 291–292. https://doi.org/10.1038/35085684.

Naresh, S. 2016. "Effect of Cooling (4 °C) and Cryopreservation on Cytoskeleton Actin and Protein Tyrosine Phosphorylation in Buffalo Spermatozoa." *Cryobiology* 72 (1): 7–13. https://doi.org/10.1016/j.cryobiol.2015.12.004.

Olson, E. N., and A. Nordheim. 2010. "Linking Actin Dynamics and Gene Transcription to Drive Cellular Motile Functions." *Nature Reviews Molecular Cell Biology*. 11: 353.

Panzetta, V., G. L. Verde, M. Pugliese, V. Artiola, C. Arrichiello, P. Muto, M. L. Commara, P. A. Netti, and S. Fusco. 2020. "Adhesion and Migration Response to Radiation Therapy of Mammary Epithelial and Adenocarcinoma Cells Interacting with Different Stiffness Substrates." *Cancers* 12 (5): 1170. https://doi.org/10.3390/cancers12051170.

Panzetta, V., G. La Verde, M. Pugliese, C. Arrichiello, P. Muto, M. La Commara, V. D'Avino, P. A. Netti, and S. Fusco. 2020. "Investigation of Biophysical Migration Parameters for Normal Tissue and Metastatic Cancer Cells After Radiotherapy Treatment." *Frontiers in Physics*. 8. https://doi.org/10.3389/fphy.2020.575906.

Panzetta, V., M. Menna, D. Bucci, V. Giovannini, M. Pugliese, M. Quarto, S. Fusco, and P. Netti. 2015. "X-Ray Irradiation Affects Morphology, Proliferation and Migration Rate of Healthy and Cancer Cells." *Journal of Mechanics in Medicine and Biology* 15 (02): 1540022. https://doi.org/10.1142/S0219519415400229.

Pedata, P., T. Stoeger, R. Zimmermann, A. Peters, G. Oberdörster, and A. D'Anna. 2015. "Are We Forgetting the Smallest, Sub 10 nm Combustion Generated Particles?." *Particle and Fibre Toxicology* 12: 34.

Puhl, D. L., A. R. D'Amato, and R. J. Gilbert. 2019. "Challenges of Gene Delivery to the Central Nervous System and the Growing Use of Biomaterial Vectors." *Brain Research Bulletin*. 150: 216.

Raoof, M., Y. Mackeyev, M. A. Cheney, L. J. Wilson, and S. A. Curley. 2012. "Internalization of C60 Fullerenes into Cancer Cells with Accumulation in the Nucleus via the Nuclear Pore Complex." *Biomaterials* 33 (10): 2952–2960. https://doi.org/10.1016/j.biomaterials.2011.12.043.

Reissis, Y., E. García-Gareta, M. Korda, G. W. Blunn, and J. Hua. 2013. "The Effect of Temperature on the Viability of Human Mesenchymal Stem Cells." *Stem Cell Research & Therapy*. 4: 139.

Ren, S., M. Wang, C. Wang, Y. Wang, C. Sun, Z. Zeng, H. Cui, and X. Zhao. 2021. "Application of Non-Viral Vectors in Drug Delivery and Gene Therapy." *Polymers* 13 (19): 3307. https://doi.org/10.3390/polym13193307.

Rother, J., M. Büchsenschütz-Göbeler, H. Nöding, S. Steltenkamp, K. Samwer, and A. Janshoff. 2015. "Cytoskeleton Remodelling of Confluent Epithelial Cells Cultured on Porous Substrates." *Journal of the Royal Society, Interface* 12 (103). https://doi.org/10.1098/rsif.2014.1057.

Rozenblatt-Rosen, O., A. Regev, P. Oberdoerffer, T. Nawy, A. Hupalowska, J. E. Rood, O. Ashenberg, et al. 2020. "The Human Tumor Atlas Network: Charting Tumor Transitions across Space and Time at Single-Cell Resolution." *Cell* 181 (2): 236–249. https://doi.org/10.1016/j.cell.2020.03.053.

Russo, C., A. D'Anna, A. Ciajolo, and M. Sirignano. 2019. "The Effect of Butanol Isomers on the Formation of Carbon Particulate Matter in Fuel-Rich Premixed Ethylene Flames." *Combustion and Flame*. 199: 122.

Russo, C., B. Apicella, A. L. Rocca, and M. Sirignano. 2023. "Fluorescent Carbon Dots Synthesis in Premixed Flames: Influence of the Equivalence Ratio." *Carbon* 201: 659–666. https://doi.org/10.1016/j.carbon.2022.09.061.

Russo, C., B. Apicella, and A. Ciajolo. 2019. "Blue and Green Luminescent Carbon Nanodots from Controllable Fuel-Rich Flame Reactors." *Scientific Reports* 9 (1): 14566. https://doi.org/10.1038/s41598-019-50919-1.

Salehi, F., H. Behboudi, G. Kavoosi, and S. K. Ardestani. 2018. "Oxidative DNA Damage Induced by ROS-Modulating Agents with the Ability to Target DNA: A Comparison of the Biological Characteristics of Citrus Pectin and Apple Pectin." *Scientific Reports* 8 (1): 13902. https://doi.org/10.1038/s41598-018-32308-2.

Schliwa, M. 1982. "Action of Cytochalasin D on Cytoskeletal Networks." *The Journal of Cell Biology* 92 (1): 79–91. https://doi.org/10.1083/jcb.92.1.79.

Şimşek, S., A. A. Şüküroğlu, D. Yetkin, B. Özbek, D. Battal, and R. Genç. 2020. "DNA-Damage and Cell Cycle Arrest Initiated anti-Cancer Potency of Super Tiny Carbon Dots on MCF7 Cell Line." *Scientific Reports* 10 (1): 13880. https://doi.org/10.1038/s41598-020-70796-3.

Sirignano, M., C. Russo, and A. Ciajolo. 2020. "One-Step Synthesis of Carbon Nanoparticles and Yellow to Blue Fluorescent Nanocarbons in Flame Reactors." *Carbon* 156: 370–377. https://doi.org/10.1016/j.carbon.2019.09.068.

Sirignano, M., D. Bartos, M. Conturso, M. Dunn, A. D'Anna, and A. R. Masri. 2017. "Detection of Nanostructures and Soot in Laminar Premixed Flames." *Combustion and Flame* 176: 299.

Sirignano, M., M. Conturso, A. Magno, S. D. Iorio, E. Mancaruso, B. M. Vaglieco, and A. D'Anna. 2018. "Evidence of Sub-10 nm Particles Emitted from a Small-Size Diesel Engine." *Experimental Thermal and Fluid Science* 95: 60.

Stoffler, D., B. Fahrenkrog, and U. Aebi. 1999. "The Nuclear Pore Complex: From Molecular Architecture to Functional Dynamics." *Current Opinion in Cell Biology*. 11: 391.

Stratton, M. R. 2011. "Exploring the Genomes of Cancer Cells: progress and Promise." *Science* 331 (6024): 1553–1558. https://doi.org/10.1126/science.1204040.

Stricker, J., Y. Aratyn-Schaus, P. W. Oakes, and M. L. Gardel. 2011. "Spatiotemporal Constraints on the Force-Dependent Growth of Focal Adhesions." *Biophysical Journal* 100 (12): 2883–2893. https://doi.org/10.1016/j.bpj.2011.05.023.

Sun, Q., K. Kanehira, and A. Taniguchi. 2018. "PEGylated TiO2 Nanoparticles Mediated Inhibition of Cell Migration via

Integrin Beta 1." *Science and Technology of Advanced Materials*. 19: 271.

Svitkina, T. 2018. "The Actin Cytoskeleton and Actin-Based Motility." *Cold Spring Harbor Perspectives in Biology* 10 (1):a018267.. https://doi.org/10.1101/cshperspect.a018267.

Svitkina, T. M. 2020. "Actin Cell Cortex: Structure and Molecular Organization." *Trends in Cell Biology* 30 (7): 556–565. https://doi.org/10.1016/j.tcb.2020.03.005.

van Zutphen, T. and I. J. van der Klei. 2011. "Quantitative Analysis of Organelle Abundance, Morphology and Dynamics." Current Opinion in *Biotechnology* 22: 127.

Tanaka, T., P. Decuzzi, M. Cristofanilli, J. H. Sakamoto, E. Tasciotti, F. M. Robertson, and M. Ferrari. 2009. "Nanotechnology for Breast Cancer Therapy." *Biomedical Microdevices* 11 (1): 49–63. https://doi.org/10.1007/s10544-008-9209-0.

Tang, D. D., and B. D. Gerlach. 2017. "The Roles and Regulation of the Actin Cytoskeleton, Intermediate Filaments and Microtubules in Smooth Muscle Cell Migration." *Respiratory Research* 18 (1): 54. https://doi.org/10.1186/s12931-017-0544-7.

Torgovnick, A., and B. Schumacher. 2015. "DNA Repair Mechanisms in Cancer Development and Therapy." *Frontiers in Genetics* 6: 157. https://doi.org/10.3389/fgene.2015.00157.

Wang, J., P. Wang, Y. He, X. Liu, S. Wang, C. Ma, X. Tian, J. Wang, and X. Wu. 2020. "Graphene Oxide Inhibits Cell Migration and Invasion by Destroying Actin Cytoskeleton in Cervical Cancer Cells." *Aging* 12 (17): 17625–17633. https://doi.org/10.18632/aging.103821.

Wang, R., and M. G. Brattain. 2007. "The Maximal Size of Protein to Diffuse through the Nuclear Pore is Larger than 60kDa." *FEBS Letters* 581 (17): 3164–3170. https://doi.org/10.1016/j.febslet.2007.05.082.

Wareing, T. C., P. Gentile, and A. N. Phan. 2021. "Biomass-Based Carbon Dots: Current Development and Future Perspectives." *ACS Nano*. 15 (10): 15471–15501. https://doi.org/10.1021/acsnano.1c03886.

Wen, Q., and P. A. Janmey. 2011. Polymer Physics of the Cytoskeleton." *Current Opinion in Solid State and Materials Science*. 15: 177.

Xiao, H., Y. Chen, and M. Alnaggar. 2019. "Silver Nanoparticles Induce Cell Death of Colon Cancer Cells Through Impairing Cytoskeleton and Membrane Nanostructure." *Micron* 126: 102750.

Xiao, Y., S. P. Forry, X. Gao, R. D. Holbrook, W. G. Telford, and A. Tona. 2010. "Dynamics and Mechanisms of Quantum Dot Nanoparticle Cellular Uptake." *J. Nanobiotechnology* 8: 13.

Yin, H., R. L. Kanasty, A. A. Eltoukhy, A. J. Vegas, J. R. Dorkin, and D. G. Anderson. 2014. "Non-Viral Vectors for Gene-Based Therapy." *Nature Reviews–Genetics* 15 (8): 541–555. https://doi.org/10.1038/nrg3763.

Zhang, J., F. Alisafaei, M. Nikolić, X. A. Nou, H. Kim, V. B. Shenoy, and G. Scarcelli. 2020. "Nuclear Mechanics Within Intact Cells Is Regulated by Cytoskeletal Network and Internal Nanostructures." *Small* 16: e1907688.

Zhang, P., J. Meng, Y. Li, C. Yang, Y. Hou, W. Tang, K. J. McHugh, and L. Jing. 2021. "Nanotechnology-Enhanced Immunotherapy for Metastatic Cancer." *The Innovation* 2 (4): 100174. https://doi.org/10.1016/j.xinn.2021.100174.

Zhang, P., J. Teng, and L. Wang. 2020. "Multiwalled Carbon Nanotubes Inhibit Cell Migration and Invasion by Destroying Actin Cytoskeleton via Mitochondrial Dysfunction in Ovarian Cancer Cells." *Aging* 12 (24): 25294–25303. https://doi.org/10.18632/aging.104130.

Zink, D., A. H. Fischer, and J. A. Nickerson. 2004. "Nuclear Structure in Cancer Cells." *Nature Reviews-Cancer* 4 (9): 677–687. https://doi.org/10.1038/nrc1430.

Zu, H., and D. Gao. 2021. "Non-Viral Vectors in Gene Therapy: Recent Development, Challenges, and Prospects." *The AAPS Journal* 23 (4): 78. https://doi.org/10.1208/s12248-021-00608-7.